

¹ Masters Thesis: The Evolution of Fault Slip
² Surfaces with Cumulative Displacement

³ Kelian Dascher-Cousineau

⁴ May 19, 2017

⁵ **Abstract**

⁶ Fault slip surface roughness determines fault strength, friction and dy-
⁷ namic fault processes. Wear models and field observations suggest that
⁸ roughness decreases with cumulative displacement. However, measurements
⁹ have yet to isolate the effect of displacement from other possible controls,
¹⁰ such as lithology or tectonic setting. We present an unprecedentedly large
¹¹ fault surface dataset collected in and around the San-Rafael Desert, S.E.
¹² Utah, United States. In the study area, faults accommodated regional ex-
¹³ tension at shallow 1 to 3 *km* depth and are hosted in the massive, well
¹⁴ sorted, high porosity Navajo and Entrada sandstones. Existing detailed
¹⁵ stratigraphic throw profile provide a maximum constraint for displacement.
¹⁶ Where cross-sectional exposure is good, we measure exact displacement im-
¹⁷ parted on slip surfaces using offset in marker horizons. Thereby, we isolate
¹⁸ for the effect of displacement during the embryonic stages of faulting (0
¹⁹ to 60 *m* in displacement). Our field observations indicate a clear compo-
²⁰ sitional and morphological progression from isolated joints or deformation

bands towards smooth, continuous and mirror-like fault slip surfaces with increasing displacement. To quantify these observations, slip surfaces were scanned with a white light interferometer, a laser scanner and a ground based Lidar. Together these instruments resolve more than eight decades of spatial bandwidth (from less than μm 's to m 's in scale). In so doing, to the best of our knowledge, we increase the existing data on published fault topographies by XXX fold (available HERE). Results indicate that roughness as defined by the power (P) at a given wavelength (λ) decreases with displacement (D) according to a power law, $P(\lambda) \propto D^{0.6 \pm 0.1}$. Trends are however subject to significant scatter. Roughness measurement associated with only maximum constraints on displacements corroborate this result—for a given displacement, minimum roughness is bounded by the later smoothing trend. In addition, we find that the maximum roughness is fixed—bounded a by a primordial roughness corresponding to that of joints surfaces and deformation band edges. Building upon our results, we propose a wear model to explain the evolution of faults with displacement. The basis of the model is supported by numerical simulations of crack initiation and growth using boundary element models Fri2D and growth by work-minimization (GROW). Our modelling provides the first insight into fault slip surface process consistent with observational constraints, i.e. fractal geometry and a nearly power-law decay with displacement, by using calling upon scale dependent strength, strength heterogeneity and scale invariant asperity failure by truncation.

⁴⁴ **Contribution of Authors**

⁴⁵ **1 Introduction**

⁴⁶ **1.1 Context**

⁴⁷ Faults are a characteristic feature of the Earth’s brittle crust. Crustal permeability,
⁴⁸ seismicity, and mineralization are just few systems upon which faults act as major
⁴⁹ controls [96, 97]. In spite of their importance, some aspects of faults and their
⁵⁰ underlying processes remain poorly understood. What are the frictional properties
⁵¹ of faults? How strong is a fault? How do faults mature as they evolve from
⁵² small to large displacement structures? Key factors such as pore pressure [?, 17],
⁵³ mineral composition [?, 28, 99] and fault architecture [25, 26] have been shown
⁵⁴ to have important roles in the behavior of faults. However, these factors often
⁵⁵ fail to explain the highly heterogeneous, chaotic and hierarchical behaviour of
⁵⁶ faults. Complex fault geometry has long been proposed as a key factor in the
⁵⁷ faulting process. However, a detailed and robust exploration of the implications
⁵⁸ thereof has only recently garnered increasing attention. This change of pace mainly
⁵⁹ owes to advances in mathematical theory behind complex natural systems [59,
⁶⁰ 60], rapid advances computational abilities enabling more complex source models,
⁶¹ technological advances in high resolution surveying tools (GPS, photogrammetry
⁶² and Lidar) and detailed field studies of fault architecture [22, 86]. Fault geometry
⁶³ has since been included as a key component of wholistic explanations for the
⁶⁴ mechanical behavior and evolution of faults (e.g. [1, 55, 86]).

⁶⁵ Fault zones generally comprise of a damage zone and fault core. The damage
⁶⁶ zone represents the halo of subsidiary fault features including smaller fault, frac-

67 tures, cleavage and veins. The fault core generally represents the zone in which
68 most of the displacement has taken place and is associated with intense comminu-
69 tions of the protolith [18, 25, 96]. Actual Slip on a fault occurs on discrete slip
70 surfaces within the fault core [?, 5, 39, 70]. These surfaces are not planar; they are
71 rough [86]. Slickenlines, corrugations, mullions and jogs are all fault slip surface
72 features which reflect the multiscale nature of fault roughness [78, 86]. Field stud-
73 ies have found common characteristics in the statistical properties which describe
74 the topography of fault surfaces. These can be summarized as follows: 1) Fault
75 surfaces topographies appear to be well defined by large fractal domains [86] ,
76 wherein 2) faults are smoother at larger length scales [?, 82] and 3) are rougher in
77 the slip-perpendicular direction than in the slip-parallel direction [56, 82].

78 Fault roughness has been demonstrated to be critical in determining fault prop-
79 erties and corresponding scaling relationships. A series of field investigations,
80 laboratory experiments, analytical predictions and numerical simulation have ex-
81 plored the heterogeneous stresses and deformation patterns around complex fault
82 geometries around single fault steps, ramps and jogs (e.g. [7, 16, 51, 62, 89]), on
83 simple theoretical fault geometries (e.g. [27, 29]), and real or synthetic faults with
84 geometrically fractal bandwidths in two dimensions (e.g. [38, 46, 76, 80] and three
85 dimensions (e.g. [63, 67, 91, 105, 106]). Direct repercussion of complex stress patterns
86 include the following: increased geometrical shear resistance [41]; increased and
87 spatially variable off-fault damage and fracture energy [27, 46, 68]; reduced stress
88 drop [106] and impeded slip budget [37]. In numerical simulations, zielke2017fault
89 reports a nearly two-fold decrease in earthquake moment release for a fault with
90 realistic roughness compared to its planar counterpart. Laboratory experiments
91 comparing smooth and rough surfaces show that with increasing roughness, friction

92 increases [8], rate and state $a - b$ slip stability increases [?], critical slip distance
93 increases and rupture nucleation dimension increases with surface roughness [?].
94 These features do appear in earthquake statistics. For example, bolstered by nu-
95 matical simulations of complex stress fields, Parsons, 2008, found that persistent
96 clusters and gaps in seismicity can be attributed to geometrical complexities on
97 faults.

98 It is therefore increasingly evident that roughness is both a fingerprint of the
99 fundamental features of- and an active agent in the faulting process [14, 21, 86].
100 In accordance, incorporating more complex sources geometries has become a more
101 frequent practice in forward and inverse dynamic earthquake rupture modelling
102 (e.g. [65, 91, 106]).

103 The measured magnitude of roughness is highly variable from one fault to the
104 other. While there has been significant progress in understanding the active role
105 of roughness in the faulting process, it remains unclear what determines the com-
106 plexity of fault geometry (e.g. [14, 22]). Sagy et al. (2007) noted a systematic
107 decrease in roughness of ‘mature’, large displacement faults compared to ‘imma-
108 ture’ faults with low displacements. Similar results have been observed along
109 reactivated joints, in laboratory experiments [36], and in compilations of fault
110 roughness analysis [?, 13]. However, these data show only weak correlations be-
111 tween fault roughness and cumulative displacement [13, 22]. These results are also
112 put in question by later experiments showing roughening with shear with normal
113 loads higher than 7.5 MPa [6]. Detailed qualitative field investigation have further
114 shown that slip geometry arises from net process between smoothing (i.e. asperity
115 failure and wear) and re-roughening (e.g. off-fault damage) [90].

116 If fault geometry changes as a fault accumulates displacement, it would have

a profound effect on fault mechanics and, correspondingly, seismology. However, relating fault roughness to cumulative displacement is not trivial. Experiments cannot perform tests with realistic roughness over large enough displacement. It is also unclear how laboratory experiments scale up to natural faults because of the fractal scaling exhibited by natural fault systems. Exhumed fault slip surfaces are rarely well preserved. In the field, obtaining well-constrained displacement estimates is contingent on the presence of precise and accurate kinematic indicators (e.g. piercing points). Additionally, combining observations over a broad range of displacements is challenging. Consequently, it is unclear whether trends observed in compilations of roughness measurements from multiple faults are directly attributable to displacement or a combination other geological factors [13]. For instance, while comparing fault surfaces from geologically diverse datasets, variations in lithology, faulting regimes, temperature and depth may all be introducing further systematic variations.

The existence of a distinction between mature and immature faults and the precise characterization of this transition has far-reaching implications. As discussed above, earthquake sources parameters are sensitive to fault roughness. Correspondingly, an evolution of roughness with displacement implies that "not all fault should be treated equally". This prediction is consistent with more efficient energy radiation measured on mature faults compared to immature faults [48]; and changes in b-values associated with fault off-set [98]. Additionally, the evolution of roughness would have a corresponding effect on the architecture of a fault zone. The geometry of the fault surface modulates the architecture of the whole fault zone [27, 46, 76]. Changes in roughness require interaction between the slip surfaces and its direct surrounding (fault core), resulting in the formation of fault

¹⁴² rock [72] and off-fault damage [46, 76]. The co-evolution evolution of the fault slip
¹⁴³ surface and the fault zone as a whole is a novel insight the maturity of fault from
¹⁴⁴ a structural point of view.

¹⁴⁵ 1.2 Fault Roughness

¹⁴⁶ The deviation of fault surfaces from planarity formally defines roughness [15]. Pi-
¹⁴⁷ oneering studies used contact profilometers to measure the roughness of fracture
¹⁴⁸ and fault surfaces along discrete profiles [15, 60, 71, 73, 86]. Combined with the sur-
¹⁴⁹ face profile of the San Andreas fault, faults were found to exhibit fractal scaling
¹⁵⁰ over a remarkably broad range of length scales ranging over 10 orders of magni-
¹⁵¹ tude—from 10^{-5} to $10^5 m$ [3, 73, 86]. Over these length scales, fractal scaling is said
¹⁵² to be statistically self-affine [59, 60].

¹⁵³ A statistically self-affine profile along x with heights $h(x)$, is invariant under
¹⁵⁴ the affine transformation:

$$\begin{cases} x \rightarrow \lambda x \\ h \rightarrow \mu h \end{cases} \quad (1)$$

¹⁵⁵ This relation therefore implies an exponential relation between the scaling, λ
¹⁵⁶ (along x), and μ (along h) such that:

$$\mu = \lambda^\varsigma \quad (2)$$

¹⁵⁷ Where ς is a constant named the Hurst exponent [82].

¹⁵⁸ Many analytical methods exist to quantify the fractal roughness of faults [?, 59,
¹⁵⁹ 84]. Possibly most intuitive of these methods is the Root Mean Squared (*RMS*)

160 as a function of scale. It is effectively a measure of topographic variance. For a
161 given profile of length L with a point spacing of Δx with deviation h from the best
162 fit line, the RMS is defined as follows:

$$RMS(L) = \sqrt{\frac{\Delta x}{L} \sum_{i=1}^{L/\Delta x} h_i^2} \quad (3)$$

163 The RMS roughness of a fault or fracture exhibits a positive power-law scaling
164 with segment length. A self-affine profile should therefore plot as a straight line
165 on a log-log plot of the RMS as a function of the segment length with a slope
166 equivalent to the Hurst exponent [84]. An alternative approach to describe the
167 fractal roughness of faults has instead been the power spectrum and variations
168 thereof (i.e. amplitude spectrum and power spectral density). By testing various
169 fractal analytical tools on synthetic profiles [84] and surfaces [?], the power spectral
170 analysis was shown to yield estimated of scaling exponent most robust to system
171 size and Hurst exponent values. For a set of discretely sampled points, the power
172 spectrum of a profile is the result of a Fourier transform. In practice it is obtained
173 using a Fast Fourier Transform algorithm (FFT). The power spectrum describes
174 a two dimensional surface profile as linear superposition of sinusoidal profiles dis-
175 cretized over a fixed frequency domain. In the frequency domain, rougher profiles
176 will have correspondingly higher amplitudes, or power. The power spectrum of a
177 self-affine profile defines a power-law:

$$P(k) = Ck^{(-1-2\zeta)} \quad (4)$$

178 Where $P(k)$ is the power at a given spatial frequency, k , C is the pre-factor and
179 ζ is the Hurst exponent [22, 59, 71, 82].

180 Early studies suggested that fault surfaces were approximately self-similar.
181 Self-similarity represents a self-affinity with a Hurst exponent is 1 [59]. The devel-
182 opments in laser scanner technology over the past decade, particularly terrestrial
183 laser scanners, enabled the detailed characterization of slip surfaces in three di-
184 mension [9, 13, 22, 49, 52, 56, 75, 78, 79]. Later studies averaging cross-sectional
185 profiles through a fault surface suggested that smaller Hurst exponen less than 1
186 may better characterize fracture surfaces and faults (e.g. [?, 22, 56, 78, 82]). Stud-
187 ies of natural mode I crack surfaces have observed radially symetric, or isotropic,
188 self-affinity with a Hurst exponent of ~ 0.8 at all scales of observation ([11, 83]-and
189 references therein). Shear, or mode II cracks (i.e. faults) were found to differ in
190 that they are anisotropic. The Hurst exponent parallel to shear (~ 0.6) is smaller
191 than that in the shear-perpendicular direction (~ 0.8) [9, 22, 56, 79]. Overall, obser-
192 vations also show that fault surfaces have distinctly smoother profiles along slip
193 direction than perpendicular to slip [?, 22, 56]. The magnitude of the roughness,
194 specified by the prefactor, C , in both directions is, however, subject to a substan-
195 tial spread in values over many orders of magnitude [13, 22]. Recent studies also
196 report a minimum length scale of grooving, a length scale at which slip surface is
197 no longer anisotropic [14, 19]. This transitions typically occurs around 4 to 500
198 μm and roughly corresponds to where the fractal scaling in the slip parallel and
199 slip perpendicular direction meet.

200 Why are slip surfaces fractal? The fractal character of worn surfaces can be su-
201 perficially explained by a range of processes. Explanations grounded in engineering
202 applications and experiments to not translate very well to natural fault systems.
203 proposition of scale dependent strength as proposed by brodsky2016scale. Using
204 the geometric scaling of slip surfaces as a record of rock strength, they argued

205 that fractal character of fault surfaces directly reflects a scale dependence in rock
206 strength. Moreover, a break in fractal scaling at the $\approx XXX\mu m$ length scale
207 is interpreted as a transitions from inelastic or brittle processes (large scales) to
208 plastic processes. This explanations is in agreement with laboratory experiments
209 that report that larger volumes of rock are, on average, weaker ...

210 Fractal characterizations of surfaces do not uniquely define a profile or surface.
211 Other statistical metrics exist and are common place in many engineering practices.
212 Specifically, examining the statistical distribution of the height measurements of
213 a surface provides insight into the contact [?], frictional behavior [?] and wear
214 processes [2].

215 define skewness, kurtosis, etc.

216 The the statistical moment is defined as follows:

217 First ($m = 1$) and second ($m = 2$) order

218 **1.3 The evolution of slip surfaces with displacement**

219 Previous work has mainly focused on mechanical wear processes as the dominant
220 mechanism of surface evolution [13, 72, 79]. Mechanical wear processes include
221 any erosive process in which volume removal by abrasion, ploughing, and other
222 fracture-induced phenomena from surfaces in sliding contact. Before further ex-
223 ploring the effects of wear in fault slip surfaces, it is worth recognizing that many
224 other processes could—and likely do—cause the slip surface to evolve with displace-
225 ment.

226 A surface can change according to the following:

227 *surface deformation*

228 *Addition of material*

229 *Removal of material*

230 Fault slip surfaces have evidence pointing to each of these processes preserved
231 in the rock record.

232 *Surface deformation* encompasses any process by which a surface changes shape
233 by the rearrangement of material (no removal or addition of mass). Both elastic
234 and inelastic processes allow fault blocks on either side of a fault to deform. At
235 the seismic time-scales, only elastic and brittle deformation can occur—whereby
236 macroscopic fault damage and micro-fractures in grains and crystals away from
237 the fault can enable strain and dissipate stress on the fault. At longer time-scales,
238 calcite twinning, pressure solution, and clay alteration can also yield similar effects
239 through plastic deformation. These short and long-time scale mechanisms define
240 the visco-elastic rheology of fault blocks.

241 It is unlikely that the rheology of the fault block and its effect on the slip
242 surface topography are significant in the evolution of the slip surface. Using slick-
243 enline orientations and fault core thickness as a proxy to the fault block rheology
244 Kirkpatrick et al. 2014, find that 1) deformation does occurs in fault block and 2)
245 there is a scale dependence to this deformation. However, this scaling is not well
246 represented in fault geometric scaling. It would rather predict a change in scaling
247 at the outcrop scale. The absence of any such signal in the topography of fault
248 slip surfaces implies that deformational processes cannot directly determine how
249 slip surfaces evolve with displacement.

250 For its part, an *addition of material* occurs as fault rock is cemented onto slip
251 surfaces—filling in geometrical concavities and effectively reducing the amplitude

of surface irregularities. Its effect is preserved in the rock record with mobile, or *fluidized*, gouge cemented and re-fractured in subsequent faulting [78, 90]. Moreover, it has been shown that discrete slip surfaces can form from the localization of shear strain within unconsolidated granular material (e.g. [24]). We speculate that the rate at which this, and similar, mechanisms redefine the geometry of slip surfaces are in large part determined by the abundance and mobility of granular material within the fault rock layer. Whether or not, the addition of wear material is a dominant agent in the geometry of slip surfaces is further investigated with field characterization of natural faults.

Removal of material is caused by mechanical wear. As fault blocks slide past each other, frictional wear is an inevitable process. Layers of comminuted fault rock, cemented or not, are direct evidence of this process [72, 87]. Wear is known to be multiscale. At small scales, grains can be plucked or broken [90]; at larger scales grains plough slip surfaces to create corrugations [85] and sidewall ripouts form [100]. All these processes fall under the definition of wear in that they involve the failure of geometrical protrusions, only these are expressed at various scales. Moreover, these have substantive impact on the surface geometry.

While wear processes are subject of a vast field of research, particularly in engineering and, particularly, tribology due to interest in manufacturing machine parts for longevity [64], its applications in the earth sciences is emergent with tests mainly conducted at laboratory scales [?, 72, 87, 103]. The only application directly grounded with field data of natural fault surfaces is a prediction of wear volume presented in brodsky2011faults.

The wear rate, the volume of wear-product produced per unit offset is broadly related to the real area of contact and loading. When two surfaces are put in

277 direct contact, the real area of contact is much smaller than the nominal surface
 278 areas because the load is supported at microscopic protrusions from a surface, or
 279 *asperities* ([?,2,12,45]). Remote loading normal to the surface causes local stresses
 280 and associated deformation at contact points. Note that as the load is increased,
 281 deformation of large asperities causes new asperities to come in contact. In its
 282 simplest form, wear rate ($\frac{\partial V}{\partial x}$) is defined according to defined to be proportional
 283 to the remote load (P):

$$\frac{\partial V}{\partial x} \propto P \quad (5)$$

284 The relation has been shown to be reasonably robust in experimentation for
 285 most materials [2]. In further detail, the size, distribution and duration of contact
 286 areas, as well as the shape of the worn particles, control the general behaviour of
 287 wear. Note that material properties are contained in a constant of proportionality
 288 referred to as the probability factor—the probability of a collision of asperities to
 289 lead to removal of material [2].

290 Following this formulation, Scholz, 1987, proposed that wear rate for faults is
 291 linearly related to displacement and an inversely related to hardness. The displace-
 292 ment relationship is in reasonable agreement with laboratory experiments [104] and
 293 measurements of natural fault rock thickness [77, 95]. The hardness dependence
 294 is difficult to test given uncertainties in both fault rock thickness and hardness
 295 scholz1987wear. The simple formulations forwarded by archard1953contact and
 296 its application to faults by scholz1987wear was acknowledged to have serious lim-
 297 itations in their applications to natural faults. Specifically, scholz1987wear raises
 298 concerns about the surface geometry of real fault, and about the scaling and ef-

299 fectiveness of wear processes such as grains plucking and fault rock abrasion.

300 Building off of experiments on engineering metals [74] and ceramics [57], power1988roughness,
301 wang1994wear new fault wear model integrated a ‘running-in’ component which
302 exponentially decays towards steady-state. This behaviour intruced a discrete
303 such that the volume of fault rock produced (V) can be expressed as a function of
304 displacement (x) according to:

$$V = \beta [1 - \exp(-nx)] + Kx \quad (6)$$

305 Where β , n , and K are constants.

306 A running-in stage is though to reflect effect of surface roughness. This later
307 formulations was supported by a semi-analytical formulations of asperity failure
308 and rotary shear experiments. However, in line with comments in Power et al.,
309 1988, we propose that this running-in stage on real faults is likely to be substan-
310 tially different for faults where fractal topography implies that new larger asperities
311 will come into contact with increasing displacement. Laboratory experiments have
312 limited fractal bandwidth. Shear boxes are limited to sample length; rotary shear
313 apparatus are limited to their circumference length. We highlight that wear pro-
314 cesses controlling the behaviour laboratory scale experiments are likely inadequate
315 for natural faults. These may instead reflect relict behaviour issuing from limited
316 fractal bandwidth and emplacement of mobile gouge layers buffering the surfaces.

317 It is clear that the fractal nature of fault surfaces is important to reconcile
318 with a model of wear. Concepts of fractal scaling, strength heterogeneity and
319 scale dependent strength are poorly captured by the current literature. Additional
320 insight from field observations are needed to better understand fault slip surface

processes. To date, notwithstanding preliminary efforts by Brodsky et al., 2011, linear scaling between fault rock thickness and displacement is nearly the only grounding field evidence for existing wear models (i.e. [72, 87, 103]). As pointed out by many authors [10, 40, 95] the scaling is contingent on highly uncertain and ambiguous measurements. Overlooking difficulties and/or inconsistencies in determining displacement, the representative fault rock thickness is difficult to measure given variations of in thickness (often many orders of magnitude, even for a single outcrop), inconsistent definitions of the measurements across the literature, and potential breaks in scaling for certain faults.

The lack of a model grounded in more field observations, quantitative data and theoretically consistent with our current understanding of fault slip surfaces is a blaring knowledge gap that we seek to fill in this study.

1.4 Faulting in Sandstone

Faults in the well sorted Navajo and Entrada Sandstones in the San Rafael desert provide an ideal natural laboratory for the study of fault maturation. These have correspondingly been subject of extensive study of fault mechanics (e.g. [4, 5, 42, 43, 54, 92–94] [44]). Its is however important to recognize faulting in sandstones such as the Navajo and Entrada units do have some peculuaritie that are worth outlining. Before presenting the tectonic and geological context of the the San Rafael desert, we first provide a brief overview of the existing litterature covering the nucleation, growth and coalescence of faults in sandstones with a specific focus on the areas presented in this study.

Two fault nucleation models exist faults in sandstone [4, 35], the first model

344 is based on the localization of strain along deformation bands and deformation
345 band clusters. Deformation bands are a characteristic feature of high porosity
346 sediment [4,5,44]. Deformation bands define sinuous sheets which localise strain in
347 zones typically less than a few millimetres in thickness [44]. Strain is accommodated
348 by the run-away crushing of sedimentary grains and the concomitant collapse of
349 pore space. Strain across deformation bands is typically in shear [44]. Shear
350 strain accommodated across a single deformation band is typically on the order of
351 millimetres. With increasing shear strain, deformation bands coalesce in localized
352 zones called deformation band clusters. It is characteristic for deformation bands,
353 and deformation band clusters to protrude out of outcrop because of differential
354 weathering. Field studies show that faults form in or along these deformation band
355 clusters [4].

356 The second nucleation mechanism relies on the reactivation and coalescence
357 of regional mesoscopic joint sets [35, 66]. Subsequent deformation leads to the
358 formation of additional joints, sheared joints, zones of fragmentation, and, finally,
359 through going slip surfaces enableb be the likage of splay fractures and joints
360 (see figure [?]). This faulting mechanism is typically associated with more intense
361 becciation and

362 The models have since been shown to be endmembers for the formation of faults
363 in the High porosity sandstone such as that of the Navajo Desert presented in this
364 study . Moreover, these mechanisms can act in unison and result in relatively
365 complex overprinted architectures [35].

366 The maturation of faults in the Navajo and Entrada sandstones, and similar
367 units in the region is particularly well recorded. In these units, the formation
368 of pristine, slickensided slip surfaces is common and seemingly does not require

369 large displacement form [4, 5]. While the evolution of slip surface with siplace-
370 ment is not described in these field area (as will be done in this study), there has
371 been substantial work describing the evolution and growth of damage zones with
372 displacement which report roughly linear scaling laws over 0 to 50 meters of dis-
373 placement [34, 92, 93]. Also, while it was typically though that defomation bands
374 pre-date the formation of faults [4, 5], it was shown that later generations of defor-
375 mation bands also form as a fault damage feature. The spatial density of deforma-
376 tion bands and fault damage rapidly decreases with increasing distance from the
377 fault according to a power law away from the center of the fault zone [92, 93].The
378 same field investigations reported no clear displacement scaling for fault core or
379 fault rock over displacements ranging [92, 95].

380 1.5 Tectonic Setting

381 The San Rafael Desert hosts a sequence of gently dipping marine and sub-areal
382 sedimentary rocks deposited from the Pennsylvanian to the Jurassic (see Figure 2).
383 The San Rafael Desert is part of the San Rafael Swell, a monocline that formed
384 when these sediments were uplifted as a passive drape fold above a reactivated
385 basement reverse fault during the Late Cretaceous Laramide Orogeny [50, 102]. In
386 turn, the swell is part of the broader Colorado Plateau [50]. Networks of joints and
387 normal faults caused by Laramide activity cross-cut the sedimentary sequence and
388 accommodate North-South extension [4,50]. Within the San Rafael Swell, we focus
389 the following field locations: 1) the Chimney Rock Fault Array (Navajo Sandstone)
390 [35,54,58], 2) the Big Hole fault (Navajo Sandstone) [92,93], 3) faults outcropped
391 in the Iron Wash (Navajo Sandstone) [4,5] and 4) a network of deformation bands

392 and faults near Goblin Valley State Park [4, 5, 42, 43] (Entrada Sandstone) (see
393 figure XXX). Table ?? present detailed descriptions of the Navajo and Entrada
394 sandstone units.

395 Advantages of theses field locations are manifold. First, the nearly pure quartzite
396 lithology, extensional tectonic regime, depth (2-4 km or 40-80 MPa), temperature
397 (estimates range from 45-90 °C) of activity, and faulting mechanism are all rela-
398 tively consistent across all field areas [102]. Consistency in these parameters is key
399 to isolating the effect of displacement on the fault roughness and is missing in any
400 previous similar study of fault slip surfaces [13, 79]. Moreover, both field locations
401 exhibit well preserved fault surfaces that are exposed and accessible (see Figure
402 3).

403 The Chimney Rock fault array is an orthorhombic set of faults that crops out at
404 the northern end of the San Rafael Swell ([35,54]). Two sets of oppositely dipping
405 normal faults crop out at the surface with preserved fault scarps. WNW-striking
406 faults have clear evidence for fragmentation and are aligned with pre-existing joints
407 and have correspondingly been interpreted to have formed by shear reactivation of
408 joints, conversely ENE-striking faults have relatively more abundant deformation
409 bands and show nearly no evidence of fragmentation and where therefore inter-
410 preted to have formed from deformation bands (Davatzes, 2003). Exposure is very
411 good, faults are abundant and have well preserved fault surfaces [102]. The Chim-
412 ney Rock fault array has studied to better understand of fault geometry [92, 93],
413 permeability [94] and kinematics [35, 54, 54, 58]. As a result, detailed maps of the
414 fault array have been produced (e.g. [58]) . In addition, by using measurements of
415 the separation between footwall and hanging wall cutoffs of sedimentary horizons,
416 entire displacement profiles have been measured for faults with a wide range of

⁴¹⁷ displacements ([32, 58, 92, 93]). The Big Hole fault is located roughly 10 km to
⁴¹⁸ the South-East of the Chimney Rock Fault Array. While not explicitly part of
⁴¹⁹ the fault array, the Big Hole fault shares a nearly identical geological setting. The
⁴²⁰ Big Hole fault has been extensively studied in detail as an analog to hydrocarbon
⁴²¹ reservoir-scale faults. Measurable displacements on the exposed fault range from
⁴²² 8 m to 39 m [92, 93].

⁴²³ Contrary to other field areas, Iron Wash, in the Navajo sandstone has not
⁴²⁴ featured a series of studies. However, it was mapped in detail by Aydin, 1977.
⁴²⁵ The area host a variety of normal, oblique and transform fault. Faults exposed
⁴²⁶ at Iron Wash are part of the Hawk's Nest fault system. The system has been
⁴²⁷ proposed to be related to the San Rafael Swell uplift [50]. Mapped displacement
⁴²⁸ range up to 80 m of offset. There are no large meters-scale slickensided surfaces.
⁴²⁹ However, it is possible to uncover small pristine slip surface sample on freshly
⁴³⁰ parted surfaces using a hammer and chisel. Here, displacement measurement are
⁴³¹ readily obtainable by using the upper horizon of the Navajo sandstone, easily
⁴³² distinguishable due to an disconformable contact also marked by a change in rock
⁴³³ color.

⁴³⁴ Large networks of deformation band faults outcrop near Goblin Valley State
⁴³⁵ Park on the southeastern margin of the San-Rafael Swell ([5]. This locality com-
⁴³⁶ prises areas mapped in detail known as Molly's Castle and Horse Creek [4]. Because
⁴³⁷ deformation bands dramatically alter the local permeability structure, Goblin Val-
⁴³⁸ ley has been extensively studied in light of fault nucleation and the implications for
⁴³⁹ hydrocarbon circulation (e.g. [43, 101]). At Goblin valley, deformation band clus-
⁴⁴⁰ ters outcrop in iconic centimeter- to meter-sized slabs. These are often bounded
⁴⁴¹ by discrete slip surfaces [5]. Offsets in sedimentary beds have allowed previous

⁴⁴² studies to obtain detailed displacement measurements (e.g. [88]).

⁴⁴³ Together, these field locations offer the chance to survey well-preserved fault
⁴⁴⁴ surfaces that have hosted displacements from embryonic stages to 55 m of displace-
⁴⁴⁵ ment. Moreover, novel to this study, we are able to survey multiple expressions
⁴⁴⁶ of a single fault's surface with various displacements according the displacement
⁴⁴⁷ profile of the fault.

Table 1: Description of lithologies featured in this study [4]

	Navajo	Carmel	Entrada
<i>Age</i>	<i>Lower Jurassic</i>	<i>Middle Jurassic</i>	<i>Late Jurassic</i>
<i>Origin</i>	<i>Wind blown</i>	<i>Marine</i>	<i>Wind blown</i>
<i>Thickness</i>	$\sim 150\text{ m}$	$\sim 50\text{ m}$	$>150\text{ m}$
<i>Rock types</i>	<i>Sandstone, limey sandstone</i>	<i>Limestone, sandstone, siltstone, shale and Gypsum</i>	<i>Cross bedded sandstone, siltstone and shale</i>
<i>Composition</i>	$\sim 90\%$ quartz, 10% feldspar grains trace <1% ferromagnesia minerals calcite and silica cement		Quartz, feldspar and ferromagnesian minerals clay, calcite and quartz cement
<i>Mean Grain Size</i>	$\sim 0.05\text{ mm}$		$\sim 0.1\text{ mm}$
<i>Outcrop</i>	<i>Chimney Rock Big Hole Iron Wash</i>	<i>Chimney Rock</i>	<i>Iron Wash Molly's Castle</i>

Loca- tion	Lithology	Description	Displacement Constraints
Chim- ney Rock Fault Array	At the contact between the Navajo Sandstone and the base of the Carmel Unit	Orthorombic set of normal faults with preserved faults scarps of Navajo Sandstone	Displacement profiled of stratigraphic throw constrained by offset on a Carmel Limestone Marker Horizon by Maerten et al., 2000.
Big Hole Fault	Navajo Sandstone	One single large normal fault structure partitioning displacement on two major strands traceable for kilometers through a river wash with scarp exposure, and strike parallel/perpendicular cross-sectional exposure	Displacement constrained using the top Erosionally competent horizon at the top of the Navajo by Shipton and Cowie, 2003 and directly where possible.
Iron Wash	Navajo Sandstone	Network of normal and strike-slip cross-cutting faults. Little scarp exposure but has good cross-sectional exposure with fresh slip surfaces (using hammer and chisle)	Displacement mostly constrained by direct measurement of offset in the Upper Navajo horizon.
Molly's Castle	Entrada Sandstone	East-West striking network of normal faults and ubiquitous deformation bands. Well preserved slip surfaces broadly	Displacement constraints available in places from mapping by Aydin (1978) and directly measured using various marker

Table 2: Table caption

450 **2 Objectives**

451 This study fills a fundamental knowledge gap in the field of structural geology
452 and earthquake mechanics. While it is increasing evident that fault roughness
453 is an important agent in the earthquake process, it is still unclear what defines
454 the magnitude and large spread in roughness of fault slip surfaces. To do so, we
455 test the two following hypotheses: 1) fault slip surface geometry is defined by its
456 displacement history wherein 2) wear is the dominant mechanism of slip surface
457 evolution.

458 These hypotheses are tested with three lines of inquiry:

- 459 1. investigation of fault architecture and microstructure of faults in the San
460 Rafael Desert, Utah (section ??). Observations have a specific focus on
461 recording qualitative changes from zero displacements structures such as de-
462 formations bands and joints, to small displacement faults (centimeters of
463 displacements) and finally to larger faults (meters of displacement). We also
464 pay careful attention to the mechanisms that alter the slip surface geometry.
- 465 2. geometric analysis of pristine fault surfaces preserved in the San Rafael
466 Desert , Utah, using scan data aquired in the field using a Lidar and a
467 laser scanner, and in the laboratory using white light interferometry (section
468 ??).
- 469 3. numerical modelling failure of asperities using Boundary Element Modelling
470 (BEM) applied to frictional faults in two dimension (Fric2D - [30,31,33,81])
471 and crack growth by work-minimizations (GROW - [61]) (section ??).

472 Building upon the results from each component, we propose a wear model for

473 fault surfaces. This model calls upon scale dependent strength, strength hetero-
474 geneity and scale invariant asperity failure processes (section ??). Note that links
475 the scans of fault slip surfaces, Matlab scripts to process and analyse slip surfaces
476 and detailed documentation is available in the appendix.

477 **3 Field observations and Microstructure**

478 We first report on the architecture of faults cutting the Navajo and Entrada Sand-
479 stones with a specific focus on the evolution from zero-displacement structures
480 such as joints and deformation bands to large offset structures with polished slip
481 surfaces and accompanying fault rock lithologies.

482 **3.1 Zero-Displacement Structures**

483 The characteristics and surface morphology of the local zero-displacement fea-
484 tures are especially relevant to our analysis as they represent the initial, zero
485 displacement, roughness of faults in the study area. This is fundamental to
486 understanding the integrated maturation path of slip surfaces to larger displace-
487 ments [72].

488 **3.1.1 Deformation Bands and Deformation Band Clusters**

489 In outcrop exposure deformation bands are sinuous white lineaments. The sin-
490 uosity and the variability thereof both are notably higher than that of faults.
491 Accordingly, the trace of single deformation bands can be nearly as linear as small
492 faults; but can also form very arcuate paths. We note that isolated deformation
493 bands, far from faults, are typically less sinuous than those near faults and zones

494 of densely packed deformation bands. We observe a range in thickness for defor-
495 mation bands of 1 to 5 millimeters in thickness. Maximum observed shear offset
496 across a single deformation band is 10 cm but is more typically on the order of a
497 few milimeters. Corresponding maximum shear strain is on the order of 10, but
498 typically is on the order of unity as reported in fossen, 2007

499 Deformation bands often protrude out of outcrop as thin sheets (see figure
500 2). The edges of the sheet are coated with single layer protolithic grain. A faint
501 anisotropy, whereby the dip-direction (parallel to strain) is smoother than the hori-
502 zontal direction (perpendicular to strain), is perceivable on the edges of protruding
503 deformation band sheets.

504 In thin-section, bands are associated with a gradational reduction in grains
505 size and an increase in angularity compared to the protolith (see figure 1). Along
506 with the reduction of grain size, intra-granular fracture are much higher, grains
507 are better packed and less porous.

508 Deformation band clusters contain groups, or clusters, of nearly co-planar, mu-
509 tually cross-cutting individual bands. The clusters are dense networks of anasta-
510 mozing deformation bands. The clusters range in thickness from a few millimetres
511 to tens of centimetres in width, often outcropping as slabs up to meters in height.
512 Clusters commonly form in upright conjugate pairs.

513 Deformation bands clusters have well defined edges. Given differential weath-
514 ering, particularly characteristic for the Goblin Valley area, deformation bands
515 form large meter-scale slabs. The exposed edges of deformation band clusters
516 have distinctly corrugated and "lumpy" morphology (see figure 3-left). The cor-
517 rugation is better defined than in individual deformation bands. The dip parallel
518 rake of the corrugations is in general agreement with the normal, dip-slip, local

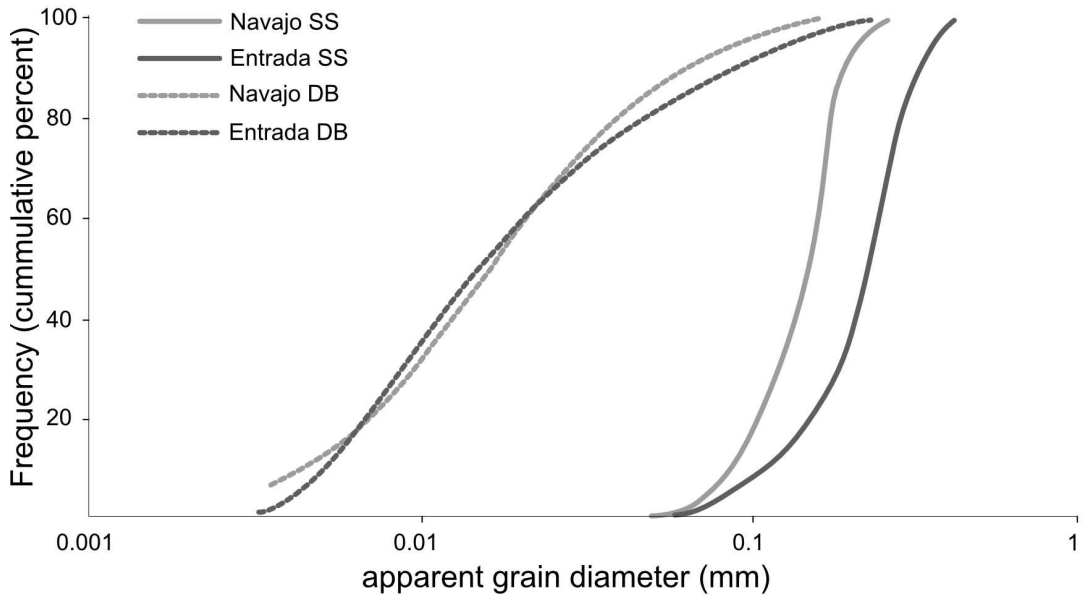


Figure 1: Grains size reduction of crushed grains within deformation bands relative to the undeformed sandstone units, the Navajo and Entrada sandstones. (figure adapted from Aydin, 1978)

519 kinematics. As is the case for individual deformation bands, edges of the defor-
 520 mation band clusters are always coated with a cohesive, single grain-thick layer of
 521 sand grains from the host sandstone. There is a clear directional asymmetry along
 522 the direction of shear whereby steep faces are in the direction of shear offset and
 523 shallowed faces are in the opposite directions (see figure 3). The asymmetry on
 524 the hanging-wall edges of the slabs is inverted on the foot-wall edges likely indi-
 525 cating an association with the overall kinematics of the clusters. Texture related
 526 to deformation band clusters are poorly captured in thin section because the size
 527 of any structural components exceeds the practical size of sections.



Figure 2: Example of single deformation bands protruding out of outcrop. A small deformation band cluster is also visible in the background.

528 **3.1.2 Joints**

529 Subvertical joints sets are a common feature of every locality. Joint sets are best
 530 defined in the upper Navajo units and lower Carmel limestone pavements. The
 531 abundance of joints increases near faults. Joints surface can be very large- effec-
 532 tively defining cliff faces 10's or even 100's of meters in size. Joints are better
 533 defined in the Navajo and Carmel Unit than in the Entrada. While spacing be-
 534 tween joint in the Carmel pavements is tight (on the order of 10 cm), the spacing
 535 in the Navajo appears to be much larger (1 m or more). Joint surfaces are notably
 536 smoother than deformation bands, but rougher than slip surfaces. Salient mor-

537 phological features on joint surfaces are the plumose structures relict from fracture
538 growth and fabrics aligned with cross-bedding horizons.



Figure 3: Left: Example of the edge of a deformation bands cluster at Molly's Castle. Note the "lumpy" morphology and an clear vertical directional asymmetry. Right: Cross-sectional view of a deformation band cluster with tens of centimeters of shear offset. It is unclear whether there is a through going slip surface localizing displacement. It is, however, definitely not on the edge of the cluster.

539 **3.2 Slip Surfaces**

540 Slip surfaces in the Navajo and Entrada sandstones are most readily identifiable
541 by their relatively planar and polished morphology with a reflective or even vitre-
542 ous polish. Striations and grooves on the slip surfaces mark the direction of slip.
543 In cross-sectional exposure, slip surfaces are discrete, through-going and smooth
544 relative to their zero-displacement counterparts. A sharp interface, separated by a
545 sub-mm thick layer of incohesive white powder bounded by two vitreous surfaces.
546 Thin milky white layers, less than a few centimetres in thickness, typically flank
547 slip surfaces. These are in turn, within dense network deformation bands. The slip
548 surfaces often cross-cut or bound deformation band clusters and the deformation
549 bands within them. Perpendicular profiles are notably more sinuous than slip par-
550 allel profiles. Slip surfaces are incohesive, and readily form a parting surface.(see

551 figure – figure similar to that in Jamies notes)

552 Slip surfaces are only preserved in the Navajo and Entrada Sandstones. For
553 example, in spite of good exposures in prospecting pits and careful inspection of
554 the slip zone, Navajo-Carmel contact at the Chimney Rock fault array does have
555 preserved slip surfaces in the Carmel Unit. It is unclear whether this indicates that
556 the Carmel units is more susceptible to erosion and/or alteration; or if a polished
557 finish is only a feature of the quartzite sandstones.

558 Thin section observations reveal a layered micro-structural architecture of the
559 faults rock locally bounding slip surfaces. The following succession, ordered ac-
560 cording to distance from the slip surface is typical for slip surfaces in sand stone: 1)
561 a very fine grained ultracataclastic layer, 2) a broader cataclasite layer (sometimes
562 absent) and 3) a deformation band zone, the density of which gradually decreases
563 into 4) the relatively intact protolith with disparate deformation bands.

564 The ultacataclasite is continuous, nearly always bounds the slip surface, and
565 ranges from sub-milimeter to 2 milimeters in thickness. Texturally, the layer tex-
566 turally overprints and cross-cuts all other layers. From visual assessment, the
567 grain size distribution has a steep but continuous (no clast/matrix distinction) fall
568 off with most grains being unresolvable at 400 fold magnification. Larger grains
569 do not exceed 10's of micron - significantly smaller than protolithic intact grains
570 which are on the order of 100's of micron. Grains have a large diversity in angu-
571 larity ranging from sub-rounded to angular. We were unable to find fragmented
572 counterpart within the ultracataclasite. This is indicative that the layer was likely
573 fluidized [69]. There are partially offset survivor grains which could be interpreted
574 as fragmented counterparts, however, these results from shear offset of fractures
575 through-going the entire unlacataclastic layer. These fractures and grains they

576 partially offset are instead indicative of cycling between healing and brittle failure
577 postdating the formation of the fluidized ultracataclastic layer. Ultracataclasite
578 layers preserve a faint, potentially compositional, foliation oblique to the fault.
579 Interpreted as S-type foliations, the kinematics from the flow banding are consis-
580 tent with sense of shear of grains protruding into the ultracataclasite and partially
581 sheared off. Previous work has shown no notable change in relative abundance of
582 major elements, silicon, calcium, potassium and sodium, of the undeformed sand-
583 stones [4]. We do however observe an increase in concentration in opaque oxides
584 near the slip surface.

585 Scattered Electron Microscopy (SEM) reveals

586 A sharp, irregular and discontinuous interface juxtaposes the cataclastic layer
587 to the ultracataclasite. The interface is characterized by a distinct difference in
588 grain size and spatial arrangement. Past this transition, grains are larger and
589 sometimes preserve damaged but intact sedimentary textures from the sandstone.

590 The interface between the ultracataclasite and the cataclasite is more irregular
591 than the slip surface. The irregularity is broadly associated with the following
592 two distinct length scales: the grain scale and the 'scalloping' length scale (see
593 figure 5. Grains at the interface are typically truncated such that their tops are
594 completely flattened. The transition towards flattened grains is well captured at
595 various different stages by instances where grains protruding into the ultracata-
596 clasite are still intact. ordered from least damaged to most damaged, we see the
597 following: 1) grains that protrude into the ultracatclasite with little to no damage
598 Other grains we evidence of healed internal cracks, 2) grains with various stages
599 of micro-cracking and fractures, with fracture orientations roughly parallel to the
600 slip and with some very small shear offset and, sometimes, rotation and 3) fully

601 cracked grain with the fragmented counterpart rotated along slip or completely
602 missing missing. While most of the fractures are only intra-granular, some frac-
603 tures can readily be projected into neighbouring grain.

604 A larger millimeter scale geometry can be traced from linking fractures. Both
605 ends of the fractures abut in the ultracataclastic layer with shallow obliquity (15°),
606 such that the crack follows an arcuate path with an overall 'scalloped geometry'.
607 The occurrence of these fractures seem to be anticorellated with the thickness of
608 the ultracataclasite. Again, this geometry is recorded at various stages ranging
609 from the alignements of multiple fractures within the catacla

610 In contrast to the ultracataclasite, the original grain geometry is sometimes still
611 discernible in the cataclasite. Grains size within the cataclasite layer is spatially
612 variable with bands or lens' of larger grains separated by finer, more angular grains.
613 These layers are texturally similar in overall geometry to deformation bands have
614 much smaller grains.

615 This cataclastic layer thickness is highly variable. It typically ranges from
616 millimetres to centimetres. Variability is directly associated with splay features
617 which intensify mechanical damage around the fault. Its thickness on either side of
618 the slip surface is often highly asymmetric. The layer is not always present. When
619 it is absent, the fault, still bounded by a thin ultracataclasite, directly transitions
620 into the intact host.

621 For certain faults, dark oxide filled fractures up to a few centimetres in length
622 abut steeply into the slip surface and over-print other fault-related textural fea-
623 tures. These are characteristically consistent with dynamics tensile cracks. If this
624 interpretation is correct, they would indicative of seismic rupture velocities.

625 The evolution of slip surfaces with displacement is qualitatively apparent.

626 Faults with small displacements (centimetres of offset) are distinctly different than
627 larger displacement faults (meters of offset). They are 1) visibly more sinuous, 2)
628 laterally discontinuous, 3) less polished, instead, having a dull lustre, and 4) not
629 bounded by well-defined gouge or cataclasites layers bounding the slip surface
630 visible in the field. The minimum observed offset across slip surfaces was approx-
631 imately 0.5 cm. It is unclear whether this lower bound is a mechanical transition
632 between deformation with deformation bands and slip on a discrete slip surface.

633 Our observations suggest that a single surface does not always accommodate
634 the bulk of the fault offset. Instead, fault zones often have many slip surfaces,
635 sheared joints and splays which partition offset.

636 Certain slip surfaces do accommodate the overwhelming majority of fault offset–
637 displacement accommodated by smaller neighbouring discontinuous slip surfaces
638 is minimal (Shipton, XXX). Based on observations from previous workers and
639 those made in this study where larger displacement slip surfaces are unambigu-
640 ously identifiable, we generalized the characteristics of large offset slip surfaces for
641 the Navajo and Entrada Sanstones as follows:

- 642 • *Large displacement slip surfaces are more discrete and planar.*
- 643 • *Larger displacement slip surfaces are not cross-cut by deformation bands or*
644 *more sinuous and discontinuous slip surfaces*
- 645 • *large displacement slip surfaces are nearly cohesionless and forming easy*
646 *parting surfaces*
- 647 • *Large displacement faults have a very vitreous finish;*
- 648 • *Large displacement slip surfaces are typically in the center of a damage zone.*

649 **Damage is an inevitable consequence of displacement and the ac-**
650 **companying mismatch that accumulates. Damage at the field locations**
651 **in this study is expressed as comminution (e.g. cataclasite and gouge),**
652 **fragmentation (e.g. breccia, splay joints) and shear deformation (specif-**
653 **ically deformation bands).**

654 In this study, we refer to *fault rock* as rocks associated with a fault (Snoke et
655 al. 1998). The faults in our study area display a very diverse range in fault rock
656 lithologies, ranging from fine-grained cataclasites to massive bodies of breccias (up
657 to meters of thickness).

658 Fault rock consistently bounds slip surfaces—often asymmetrically. However,
659 observations at the outcrop scale (10's of meters) both along the strike and dip
660 indicate that both the lithology and thickness of the fault rock are highly heteroge-
661 neous and are subject to large variability. These observations are consistent with
662 more detailed fault architecture mapping conducted by Shipton et el., 2002.

663 We do not observe a clear and tractable relation between fault slip surface
664 displacement and faults rock thickness. This is big part a result of difficulties in
665 defining a clear fault rock thickness criterion which well encapsulates the variety
666 of faults rocks – a challenge well highlighted in (Shipton et al., 2006).

667 * this stuff is left over's from editing and moving things around

668 Healed Gouges

- 669 - the spot at big hole
- 670 - iron wash (powder between the surface)
- 671 - micro-structure
- 672 - prospecting pit
- 673 - typically on thinned sections of the fault rock (near the slip surface) Catacl-

674 asites . . .

675 - big hole sample with slip surfaces on both sides of the cataclasite

676 - micro-structure - Breccias . . .

677 - thick sections of the Breccias occur lenses which range from cm's to meters in

678 thickness. Breccia clasts are typically poorly sorted and can be very coarse with

679 clast up to 10 cm in diameter. Clasts show indications for multiple generations

680 of brecciation.

681 Thin Quarts lens - iron wash

682 Systematic associations between fault rock and fault structure exist. For in-

683 stance, Davatzes et al., 2002 reports of a systematic association between the fault

684 rock lithology and the orientation of the fault set. Namely, the orthorhombic fault

685 set striking WNW has systematic association with fragmentation—fault breccias;

686 conversely the ENE fault set rather has slip surfaces cutting through deformation

687 band clusters (see figure ??). This relation was speculated to be the result of

688 contrasting genetic mechanism. The WNW set is the result of the reactivation of

689 regional joints. In contrast the ENE fault set is the the result of clustering and

690 anastamosing deformation bands acting as a catalysing agent to the formation of

691 a faults. In this study, we observe clear instance of lithological contacts being

692 associated with brecciation (photo at iron wash where the top of the Navajo is

693 brecciated and quickly reverts to a single fault strand. More over, large breccia

694 bodies are clearly related to points where faults are cross-cutting each other at

695 high obliquity as is often the case at the Chimney Rock fault array and

696 Complicating factors:

697 Associations between brecciation and lithological contacts . . .

698 Associations between brecciation and cross cutting faults . . .

699 For an extensive review and description of the faults in the Navajo and Entrada
700 sand stones refer to Aydin's thesis.

701 **3.3 Interpretation of field observations and roughness mea-
702 surements**

703 Cross-cutting relationships reported bot in this study and in previous work on
704 faults in the Navajo and Entrada units of the San-Rafael swell are particularly
705 informative. Large displacement slip surfaces are not cross cut by deformation
706 bands and more sinuous slip surfaces. However, large displacement slip surfaces
707 do cross-cut clusters of deformation bands and more sinuous slip surfaces. This re-
708 lationship is indicative of a clear evolution of the fault architecture by 1) localizing
709 displacement and 2) smoothing out slip surfaces.

710 Faults zones with larger offset are associated with larger damage zones and
711 more slip surfaces. This is particularly telling fact when with the observation that
712 small displacement slip surface do not cross cut larger displacement slip surfaces.

713 The cross cutting relationship implies that either slip either smaller less con-
714 tinuous slip surfaces pre-date the onset of the larger offset slip surface or that the
715 they splay off of it. However, we can reject the former as a possible mechanism as
716 it does not account for the increased density of slip surfaces on larger offset fault
717 zones. This implies that they either form directly from the stress heterogeneities
718 induced by the roughness of larger displacement slip surfaces.

719 Slip surfaces pre-dating large The former case stress heterogeneities from active
720 slip surfaces induced by fault roughness.

721 faults are smoother than joints or deformation bands

722 At the grains scale, grains are truncated, not ‘plucked’.

723 more linear fault traces where not offset by wavier fault traces

724 **The textural transition between the ultracataclasite and the catacl-**
725 **asite is best explained by dynamic grain size reduction and wear at the**
726 **slip surface interface producing ultracataclasite which overprint more**
727 **diffuse off-fault grain size reduction through grain crushing and defor-**
728 **mation band production.**

729 4 Geometric analysis

730 4.1 Method

731 Previous efforts to correlate fault roughness to displacement were frustrated by
732 limited cliff-size exposure and bad displacement constraints, fundamental to the
733 quantitative analysis of the roughness data (i.e. [13, 22, 79]). Field methods in this
734 study correspondingly prioritize 1) slip surface quality 2) good displacement con-
735 straints 3) the number of faults scanned. Note that we do not necessarily prioritize
736 large exposure size as has been done in previous work.

737 We collected high precision, high density measurements with optical scanners
738 in the field and, later, in laboratory on collected hand samples. Every scan was
739 associated with a constraint on displacement. Moreover, we also recorded the time
740 of day, location, quality of the slip surface, strike and dip of the fault slip surface,
741 slickenline rake, and both plan and cross-sectional photographs. When permitted
742 by outcrop exposure, we recorded an estimate of the fault rock thickness. See
743 appendix for the tabulation of this data. Together, all these measurements and

744 observations should provide the necessary data to robustly explain and quantify
745 the processes through which faults mature.

746 **4.1.1 Scan Data Acquisition**

747 A scan of a fault slip surface discretizes it into a *point cloud*, a series of x , y
748 and z coordinates. We measure slip surface roughness by analysing these point
749 clouds scans. Specifically, we average the slip parallel and perpendicular spectral
750 and statistical properties across hundreds of profiles. To ensure the fractal scaling
751 is well-captured by the point cloud data, we use the following three scanning
752 instruments capturing various scales of observations: a New View 8000 structure
753 image analyzer (Zygo Corporation), a NextEngine desktop laser scanner and a
754 BLAH BLAH LiDAR. Together, these instruments offer the potential to resolve
755 fault slip surface geometry with high accuracy and precision at over nine decades
756 of length scale.

757 *make a map of each areas with the location of every scan encoded with dif-
758 ferent symbols*

759 A light detection and ranging instrument was used to resolve length-scales
760 ranging from meters down to millimetres, (i.e. LiDAR). LiDar has been used in
761 many previous studies of fault roughness as it is easily deployable in the field and
762 provides rapid means to collet very large point cloud data set. However, its use is
763 limiting as it requires exceptionally good and, accordingly, rare exposure of fault
764 surfaces that are large enough and fresh enough to not have been degraded by
765 erosion. In this study, we report 5 ??? Lidar Scans (see figure).

766 The bulk of *in situ* field measurements were made at intermediate length-
767 scales ranging from centimetres down to hundreds of microns with the NextEngine

768 desktop 3D laser scanner. The NextEngine laser scanner has a working distance
769 of 13 to 57 cm. Maximum accuracy, point cloud density and resolution are all
770 broadly function of the working distance. In this study nearly all scan where
771 measure at the optimal minimum working distance (15 cm). Accordingly, point
772 clouds measured this study are expected to have an accuracy of 0.01 cm and a
773 point density of 41 540 points/cm². surface both to industrial-grade laser scanner
774 as reference. The scanner is not exactly built to be field ready. It requires a power
775 source, low light conditions, a stable surface to sit on, limited dust exposure and
776 must be connected to a computer. Therefore, to use the scanner in the field, we
777 connected both the laser scanner and laptop to a solar powered, *Goalzero* battery.
778 The scanner was encased and padded in a reinforced cardboard box cut such that
779 the depth exactly corresponds to the optimal instrumental depth of field. The set
780 up had the added advantage of being very portable, completely removing sunlight
781 and limiting dust exposure. We report 45 scans using this field apparatus.

782 Finally, hand samples were collected and at McGill laboratories using white
783 light interferometry. Slip surface samples are cut to be roughly 1 cm². We ap-
784 ply a 4 nm platinum coating. Point clouds where then produced using the New
785 View 8000 structure image analyzer (Zygo Corporation). The instrument is an
786 optical profilometer using a non-contact method, instead using a scanning white
787 light source. The profilometer can capture surface geometry over length-scales
788 ranging from millimetres down to hundreds of nanometres by using 2.5, 10 and 50
789 fold magnification objectives. Point point-clouds are relatively small, however it
790 is possible to seamlessly stitch smaller scans together. Point clouds where bench-
791 marked to a silicon carbide mirror reference. For the purpose of this study, all
792 samples where scanned at 20 and 2.75 magnification objectives. Scans obtained

793 at 20 fold magnification where stitched together to produce sections roughly 2 by
794 4 millimetres with over 10^7 points. Scans obtained at the 2.75 fold magnification
795 are typically on the order of the sample size and have 10^6 points. The later length
796 scale nicely bridges the interferometry and laser scanner spatial resolution. We
797 report on 73 point clouds obtained with the white light profilometer.

798 **We assess the effect of erosion of slip surfaces by qualitatively com-**
799 **paring freshly parted slip surfaces with fault scarps with surfaces that**
800 **have been exposed to the elements for a long time. Weathered scarps**
801 **do preserve slip surfaces. However, these have a reddish-brown to dark**
802 **tarnish and less vitreous lustres. Sections of the slip surface are plucked**
803 **off. Severely weathered scarps develop a slip perpendicular fabric as-**
804 **sociated with conjugate fractures and deformation bands abutting into**
805 **the slip surfaces. These surfaces where not scanned. From our field**
806 **observation, it is clear that erosion has the effect of re-roughening the**
807 **slip surfaces, especially at smaller scales. We can confidently attribute**
808 **these re-roughening effects to erosion because they did not occur in**
809 **freshly parted slip surfaces. The extent of weathering and erosion was**
810 **noted and taken into account in post-processing stage on data analysis.**

811 4.1.2 Constraining displacement

812 We associate every scan with displacement constraint. At The Chimney Rock
813 Fault Array and Big Hole Fault, entire displacement and/or throw profiles have
814 been measured during previous mapping campaigns ([53, 54, 58, 92]). For the
815 Chimney Rock fault array, we use geospatial data obtained from Maerten (personal
816 communications). At big hole we used maps in [92] as reference. At Iron wash,

817 Horse Creek and Molly's Castle, Atilla Aydin's mapping identified clear offset
818 markers where available ([4]). For these field locations we use maps available in [4].
819 When necessary base maps for all field locations were digitized and georeferenced
820 using satellite images. Maps where all used the field to streamline scan data
821 acquisition. Displacement were estimated after the field campaign using GPS
822 locations collected in the field. Additional measurements using basic tape measure
823 and compass triangulation methods where also obtained in the field to obtain true
824 faults slip surface displacement.

825 Base maps only report stratigraphic throw or, in some cases, offset across fault
826 zones. However, many slip surfaces, complex networks of deformation bands and
827 sheared joints which partition offset across fault zone (see figure). We there-
828 fore make a distinction between *offset* across an entire fault and *displacement*
829 across a single slip surface. Without good marker horizons and cross-sectional
830 exposure, how stratigraphic offset is partitioned across slip surfaces is ambiguous.
831 Offset across the entire fault zone therefore only serves as an upper-bound con-
832 straint on displacement across a single slip surface slip surface. For 60% of point
833 cloud measurements, this is the best available constraint on displacement.

834 We were able to reconstruct exact displacement in the following specific cases:
835 1) if cross-sectional exposure indicates only one slip surface; 2) If cross-sectional
836 exposure is good enough to clearly indicate cutoff surface (lamella, cross-bedding
837 or lithological contact); or 3) following [25] and, locally, [92], if it is unambiguous
838 that there is a *principle slip surface* accommodating the overwhelming majority
839 of fault offset, i.e. it is continuous, it has a layer of fault rock and is unmistakably
840 more linear and sharp than any other slip surface in the fault zone.

841 Errors on displacement estimates are either reported directly for previous work

842 when available. For Chimney rock, we report $1m$ precision based on high resolution
843 GPS mapping by Maerten et al., 2001. For Big Hole, we report $5m$ precision based
844 on total station surveying by Shipton et al., 2001. For our field measurements and
845 those made by Aydin, 1977, we report conservative 10% error on displacement
846 estimates.

847 **4.1.3 Scan data Processing**

848 We use point cloud spatial statistics to characterize and quantify features of the
849 topography that could record active surface processes on faults. We developed a
850 *MatLab* work flow to entirely automate data processing from the raw *.xyz* input
851 format to the final statistical analysis:

852 1. Preprocessing

- 853 (a) manual inspection and removal of coarsest defects in built in scanner
854 software
- 855 (b) export point cloud data to *.xyz* data
- 856 (c) Import *.xyz* data into *Matlab*
- 857 (d) Very coarse Height field filter (standard deviation threshold)
- 858 (e) Rotate mean plane to horizontal
- 859 (f) Orient grid along slip direction (using power spectral analysis)
- 860 (g) re-grid to even point spacing
- 861 (h) Remove defects
- 862 i. Remove outliers in the height field (standard deviation threshold)

- 863 ii. Fractal model filter
864 iii. Remove re-gridding artefact

865 2. Processing

- 866 (a) Statistical analysis
867 i. Scale-dependent *RMS*
868 ii. Scale-dependent skewness
869 iii. Scale-dependent kurtosis
870 iv. Scale-dependent asymmetry
871 (b) Spectral Analysis
872 i. Fast Fourier Transform (FFT)
873 ii. Lomb-Scargle Periodogram

874 *make into figure, include bypasses and other recent additions*

875 Before conducting a statistical analysis scan data must be pre-processed into a
876 workable format. Scan data is a point cloud - a series of points with coordinates
877 x , y and z . Scans reported in this study typically have 10^6 to 10^7 points. In raw
878 form, the point clouds are randomly oriented, noisy and still contain instrumental
879 and physical artefacts. Physical artefacts include cracks, eroded sections, and
880 vegetation; instrumental artefacts include noise, smoothing and scattering. All
881 these features must be removed. The process of manual removal is labour intensive
882 and infeasible for a data set of the scope presented in this study. I rather opt to
883 automate this process. Only very large defects (defects that may substantially
884 effect the quality of finding a true mean plane) are manually removed.

885 The surface must first be rotated such that the mean plane is horizontal and
 886 aligned along slip. Linear trends in the data induce unwanted high frequency signal
 887 in data and also affect the quality of interpolation in upcoming steps. Thus, x , y ,
 888 z data is rotated around the axis \mathbf{u} determined by the normalized cross product
 889 between the normal vector to the mean plane of the point cloud, \mathbf{n} , and the unit
 890 vertical vector, \mathbf{n}_2 :

$$\mathbf{u} = \mathbf{n} \times \mathbf{n}_2 / |\mathbf{n} \times \mathbf{n}_2|$$

891 with the rotation,

$$R = \cos \theta \mathbf{I} + \sin \theta [\mathbf{u}]_x + (1 - \cos \theta) \mathbf{u} \otimes \mathbf{u},$$

892 were $[\mathbf{u}]_x$ is the cross product matrix of u and \otimes is the tensor product and \mathbf{I} is
 893 the identity matrix.

894 Fault surfaces are anisotropic [56]. The direction of slip is preserved in the
 895 anisotropy whereby the 'smoothest' direction is slip parallel and the 'roughest'
 896 direction is perpendicular to slip. The fault scan is rotated around the z axis such
 897 that the direction of slip is parallel to the x axis. The direction of slip is found by
 898 decimating raw data before performing spectral analysis along directions rotated
 899 by 1° increments around the z-axis, iterating through the steps of regridding at
 900 each rotation. In this radial search, roughness is quantified as the integral of the
 901 log-weighted power spectrum over the entire bandwidth of the sampled surface.
 902 The direction in which the roughness attains a minimum value is then identified
 903 as the direction of slip and subsequently used to rotated the original point cloud.
 904 The data is then interpolated onto a grid using a linear interpolation algorithm.

905 The point spacing of the grid is automatically defined by the point density over
906 the areal extent of the data:

$$\Delta x = N_{pts}/A \quad (7)$$

907 Where Δx is the point spacing, N_{pts} is the number of points and A is the
908 areal horizontal extent of the data. The later is determined using a convex hull
909 over the $x - y$ projection of the point cloud. This treatment results in the point
910 spacing of the grid to be roughly consistent with that of the original scan.

911 INCLUDE HISTOGRAMS FOR EACH FILTER

912 *Defects* include all physical surface features that are clearly not associated any
913 faulting process, *e.g.* cracks, eroded patches, vegetation, etc.. Defects are ideneti-
914 fied and filtered out using combination of thresholding methods. These methods all
915 involve identifying points or linear segments of points that are statistical outliers
916 to the distribution characterizing the entire surface.

917 The most aggressive filter implemented searches for outliers to the fractal
918 model. The filter removes entire linear segments of points with abnormally high
919 variance in the height field for the given scale of observation. For this implemen-
920 tation, I iterate over 10 filter segment length-scales. The length-scales are selected
921 using a log spacing between the 10 points and the length of the entire surface.
922 The threshold for segment removal is chosen to be four standard deviations from
923 the mean which accounts for < 0.1 percent of a normal distribution. Note that,
924 assuming a normal distribution of data for a given scale, the filter does not induce
925 a systematic bias in the mean value, since the filtering is symmetric around the
926 mean. However, surface features associated with a truly distinct mechanism of for-

927 mation, in this case cracks and other defects that will typically have much higher
928 variance, *are* be removed. This general approach ensures that defects, regardless
929 of their scale are identified and removed.

930 In some cases, abnormally flat sections are introduced into a surface height
931 field during the interpolation of sparse points. Typically, interpolation on the
932 edge on a non-convex set of points is subject to this effect. These artefacts are
933 readily identified following calculation of the surface curvature data. In the log-
934 transformed absolute value curvature field, these sections appear to be nearly or
935 exactly zero. The filter rejects point with curvatures less than $10^{-25}m^{-1}$. These
936 values are assumed to be the result of the linear interpolation scheme.

937 Finally, all scan are inspected to make sure that the pre-processing was suc-
938 cessful. The workflow fails to properly process scans that have too many defects
939 surface defects. This is because 1) the mean plane is skewed by surface defects
940 and in turn affects identifications of outliers in the height-field; and 2) the dis-
941 tinction between the fault surface and outliers becomes less distinct in the fractal
942 model. These scans were manually cleaned and oriented before re-processing them.
943 Manual changes were executed in a point cloud editing software *CloudCompare*.

944 Pre-processed scans are N by M scalar fields of fault surface topography(the
945 sitance from the mean plane) aligned with slip along the x axis. NaN values mark
946 locations where data is missing or was removed by filters. Point spacing is defined
947 the mean point density of the scan in the x - y plane.

948 We adapt the general pre-processing workflow to account for instrumental arte-
949 facts. Scans collected with the LiDAR required more extensive manual point re-
950 moval to avoid features such as vegetation, spurious outlier and large defects to
951 affect the quality of the preprocessing. Scans collected at the intermediate scale

952 with the laser scanner easily followed this workflow. Finally, scan collected with
953 the white light interferometer have little to no surface defects and are aligned
954 before scanning. Moreover, instrumental *Zygo* software automatically generates
955 point clouds in grid-form. Therefore, for these scans, most of the pre-processing
956 step are omitted.

957 **4.1.4 Statistical Analysis**

958 After pre-processing, scans discretize defect-free slip surfaces with grids with rows
959 aligned with the slip direction. We compute the power spectral density content for
960 every continuous segment of every single profile of the grid using a Fast Fourier
961 Transform (FFT). Individual spectra are interpolated onto a master frequency
962 vector. For a given frequency, the distribution of power values across the pro-
963 files through along the slip is strongly skewed (see figure xxx). The skewness is
964 attributable to the non-negative constraint on power and residual outlying pro-
965 files (defects not properly removed). To provide a more representative and robust
966 measure of maximum likelihood, we use the geometrical mean instead of the arith-
967 metical mean. Accordingly, errors represent the 1σ range in the log-transformed
968 distribution. The analysis yields one representative spectrum for each scan.

969 The spatial frequency content of slip surfaces follow a power law. This charac-
970 teristic is roughly fixed for a single slip surface regardless of the scale sampled in
971 our instrumental array. Fixed scaling and its power law form in frequency space is
972 a feature of the fractal character of fault surfaces. We can thus further distil the
973 roughness measurements using the fractal model of the fault:

$$P(k) = Ck^{-\beta} \quad (8)$$

Accordingly the entire spectral information of a scan can be summarized with the prefactor (C) and the scaling exponent (β). Determining fractal parameters from spectra is not trivial. *A priori*, the fractal model is determined using a weighted power law regression through the spectra. Weights are determined according to the inverse $1\sigma^2$ variance of the power estimates. However, confidence interval on the fit parameters are strongly sensitive to both instrumental and analytical biases (XXX schittbulh 1998). Biases induce unwanted high or low pass filters in the spectral content-amplifying or diminishing selective bandwidth. The combination of instruments and highly overlapping bandwidths provides a means to identify the affected sections and suppress methodological bias. The comparison of the power law fit through multiple heavily overlapping instrumental bandwidths to the representative spectral of individual scans highlights instrument-specific biases. In doing so, we identify conservative bounds on sections of frequency spectrum that deviated from the power law fit. For our instruments, we find that artefacts are particularly disruptive at the small scale instrumental limit. The LiDar and laser scanner are dominated by a shallower slope at the high frequency tail of the spectra which has been interpreted in previous studies as random noise (XXX). Conversely, the spectra of the scan collected using the white light interferometer have steeper high frequency tails. This artefact has not been reported in previous studies in spite of the extensive use of the instrument. This discrepancy is likely attributable to the comparatively limited and subdued use of aggressive smoothing filters both in the scan data and in the spectra our analysis. Affected bandwidths are omitted from subsequent analysis. In spite of this approach, small discrepancies in parametrization of the power law fit for a given slip surface render the extrapolation of measurements from on instrumental bandwidth to the other

999 instrumental scale of limited use. We therefore choose to report any further re-
1000 sults at the bandwidth or specific wavelength best captured by the instrumental
1001 magnification.

1002 INCLUDE A FIGURE WITH: ORIGINAL SURFACE, AUTOMATICALLY
1003 PROCESSED GRID, MANUALLY PROCESSED GRID AND CORRESPOND-
1004 ING POWER SPECTRA.

1005 identifying fractal scaling section plot of white light all magnifications compu-
1006 tational scheme to select the good section error on direct displacement estimates?

1007 4.2 Results

1008 4.2.1 Roughness measurements

1009 figures to :

- 1010 • all spectra
1011 • increasing anisotropy (two surfaces) - polar plot

1012 Figure XXX shows the all the PSD calculations obtained from the scans col-
1013 lected in this study. Consistent with previous work, we find that the PSD spectra
1014 over the entire bandwidth reported in this study generally follow a power law scal-
1015 ing (a linear relation in log-log space). This feature corresponds to the constant
1016 fractal scaling. The scaling exponent and pre-factors are calculated using linear
1017 least-squares fit of the spectra in log-log space. The Hurst exponent can then be
1018 obtained according to equation XXX.

1019 In the slip perpendicular direction, Hurst exponents range from XXX to XXX,
1020 with an average value of 0.8ish; Prefactors range from XXX to XXX with an

average value of XXX. In the slip parallel direction, Hurst exponents range from XXX to XXX, with an average value of 0.8ish; Prefactors range from XXX to XXX with an average value of XXX. Implicit to the pre-processing grid alignment, for any single scan the slip parallel direction is systematically smoother than the slip perpendicular direction indicating a clear surface anisotropy. The entire data set does however indicate an overlapping range in slip parallel and perpendicular directions. We also note that lower pre-factors are generally associated with lower Hurst exponents.

An evolution with displacement is weakly expressed in the spectral analysis but is cluttered and obscured by highly variable errors on displacements and roughness measurements. In order to highlight the effect of displacement on the surface roughness, we separate our scan data into two distinct populations. 1) Scan data with direct displacement constraint and 2) scan data associated with maximum displacement constraints. Brodsky et al., 2011, tested the validity of a power law relation between fault roughness at various specific scales and displacement. Building upon this approach, we use both data populations to test the validity and parametrization of the fit and the Implicit hypothesis that faults smooth as a function of displacement—the smoothing model. Scan data with direct displacement constraints serves as a direct test and a means to parametrize the smoothing model. For the model to be valid it must agree with further constraints imposed by data with only maximum displacement estimates.

A point defined by the maximum error bound on displacement and the roughness of the fault surface is in agreement with smoothing model if it is rougher than roughness prescribed by the model as parametrized by direct measurement. Conversely, if the point is rougher than the model prediction, it is not physically

1046 possible in the model construct. A null hypothesis would prescribe no bound on
1047 the roughness and would simply have the predicted roughness of a fault be defined
1048 by the probability distribution function of the entire roughness dataset.

1049 * probably will revisit this *

1050 Accordingly, we can roughly estimate the probability that our distribution of
1051 data relative to the smoothing model is a random element of chance according to:

$$P = \prod p(y_i > Y(x_i)) \quad (9)$$

1052 Figure shows the relation between roughness and displacement as interpolated
1053 a various scales of observation. Vertical error bars on the power spectral density
1054 are obtained from the confidence interval of the of the fractal model regression.
1055 Horizontal errorbars on displacement are defined on a case by case basis from
1056 field observations and previous work in on the fault arrays. We present both
1057 the fit through the our entire dataset (comprised of direct and upper bound con-
1058 straints on displacement) and through the the directly constrained displacement
1059 estimates. Fits are obtained using a least squares linear regression through the
1060 log-transformed data sets. In order to provide error bounds on the fit parameters,
1061 we use a full Monte Carlo simulation sampling direct displacement estimated as
1062 Gaussian distributions, upper bound displacement constrains as completely ran-
1063 dom distributions across the entire possible range of displacements and power
1064 spectral density estimates as log normal distributions. Errors represent on stan-
1065 dard deviation estimated from 10000 simulations.

1066 The weak trend across the entire dataset imply and expectation of smoother
1067 slip surfaces in fault zones which have accommodated larger displacement.

1068 Conversely the stronger trend across the well constrained data implies that an
1069 individual slip surface smooths with displacement. The smoothing exponent varies
1070 according to the different scales of observation (XXX at the laser at the centimeter
1071 scale, XXX at the millimetre scale and XXX at the micron scale). While a power
1072 law fit to the best constrained measurements is has poor fit metrics, we find a nearly
1073 perfect agreement with roughness measurements only associated with upper bound
1074 constraints.

1075 Two constraints on displacement – two data populations plot of all the spectra
1076 color coded with displacement smoothing plots: parallel - ζ all scales perpendicular
1077 - ζ all scales Hurst exponent - ζ all scales Fit for smoothing through direct data,
1078 discuss consistency with max disp data Other statistical metrics? Poly-gaussian
1079 features in the surface roughness Skewness of height field as a function of scale
1080 Null result worth reporting? Do a plot of the evolution of skewness at the grain
1081 scale?

1082 qualitative illustration of maturity

1083 4.3 Hard facts

1084 The following is a list of ‘hard facts’ that can be established from the both the
1085 qualitative and quantitative data:

- 1086 • faults are smoother than joints or deformation bands
 - 1087 – power spectrum shows that fault slip surfaces are systematically smoother
1088 than joint and deformation band surfaces at all wave lengths reported
1089 in this study (10^{-6} to 10^5 meters)
- 1090 • At the grains scale, grains are truncated, not ‘plucked’.

- The roughness of a slip surface is sensitive to its displacement history. This result is robust across multiple faults both nucleated from deformation bands and joints and variations in fault rock and host rock lithology.
- The smoothing exponent is likely more than 1 at certain scales - quote from Emily: "In all of these cases, the scatter of the data is large, but the basic result holds: the absolute value of the exponent is much less than 1."
- The smoothing rate is highest at small displacements and decreases with displacement.
- Smoothing occurs at all scales of this study
 - a slip surface from a large offset fault is more likely to be smoother
 - for any given the displacement on a fault, the smoothest slip surface roughly follows the same smoothing trend as that defined by direct displacement measurements.
- The roughness varies spatially on a slip surface - the scatter in the data exceeds the instrumental error
- the height distribution of points on a slip surface can be far from normally distributed.
- the Hurst exponent has a very large range in values (less than Zero to 0.9)
- more linear fault traces where not offset by wavier fault traces

₁₁₁₀ **5 Model**

₁₁₁₁ In this study, we utilize work minimization and boundary element numerical mod-
₁₁₁₂ elling to capture the growth of fault damage and the effect of rough asperities.
₁₁₁₃ The modelling component is motivated by the following questions: can geomet-
₁₁₁₄ rical asperities fail through shear? In so doing, how do they fail?—and what are
₁₁₁₅ its sensitivities to asperity geometry and strength? Does strength heterogeneity
₁₁₁₆ and mechanical wear by the truncation of asperities properly capture the evolu-
₁₁₁₇ tion of fault slip surfaces with displacement. These questions prompt the need for
₁₁₁₈ physically robust models that can be accomodating of complex fault or asperity
₁₁₁₉ geometries. The complexity of these geometries imply that off fault damage will
₁₁₂₀ grow in complex stress conditions— conditions that are currently poorly captured
₁₁₂₁ by simple analytical solutions (e.g. [27]). Moreover, complexities related to the
₁₁₂₂ discontinuous nature of fracture are more simply captured by boundary element
₁₁₂₃ modelling than existing finite element or finite difference models. This simplicity
₁₁₂₄ arises from need of fewer, less sparse, sets of equations to solve ([33]). Limita-
₁₁₂₅ tions of the boundary elements approach for fault modelling and off fault damage
₁₁₂₆ predictions is the difficulty of accumulating offset. Maximum allowable offset is
₁₁₂₇ roughly half the length of boundary elements. Along with this complications is the
₁₁₂₈ implicit trade off between model resolution and displacement. Approaches can be
₁₁₂₉ taken to circumvent the challenge however its development and implementation
₁₁₃₀ are beyond the current scope of this study.

₁₁₃₁ The model builds off of fric2D and growth by optimization of work (GROW)
₁₁₃₂ developed by Michele Cooke and Jessica McBeck. Fric2D solves for displacement
₁₁₃₃ and stress conditions on fault elements with prescribed constitutive behaviours

given prescribed boundary element stress boundary conditions and material properties in two dimensions. Constitutive behaviour of fault elements are defined by its static and dynamic friction, critical slip distance, and shear and normal stiffness. In turn the behaviour of the medium fault elements and boundary elements is linear elastic defined by Poisson's ratio and Young's modulus. For its part, GROW predicts fracture propagation paths. It does so by minimizing the external work on a system. As a natural analogue, the external work is the tectonic work imposed on a fault and its fault blocks, together comprising the system. The model allows for the simultaneous growth of multiple fractures. The general algorithm uses the same boundary element method as fric2D to describe the fractures–linear dislocation elements that discretize the entire length of the fault. As a crack grows, dislocation elements are added radially to the tip of the crack so as to minimize the external work on the system normalized by the crack area ($W_{ext}/\Delta A$). External work is further defined as:

$$W_{ext} = \oint (\tau u_s + \sigma_n u_n) dB \quad (10)$$

External work is readily calculated from the output of fric2D. Accordingly it is possible to iteratively test a range of directions of growth, compare the external work required, and choose the energetically preferred direction of crack growth. This process continues until stress at the tip of the cracks is not sufficient to overcome the fracture toughness. Therein lies the general algorithm of GROW.

In practice GROW utilizes almost the same inputs as fric2D. The user must specify what points are considered to be 'flaws'. Only the coordinates associated with the flaws are analysed and allowed to grow according to the GROW algorithm.

1156 The computational cost of multiple initiation points is large. Every added flaw
 1157 grows the computational cost exponentially according to the angular range and
 1158 resolution. We rather use fric2D to educate the choice of coordinated for the flaws
 1159 on the fault.

1160 Stress conditions are assessed along the fault elements. Normal (σ_{11}), shear
 1161 ($\sigma_{12} = \sigma_{21}$) and tangential (σ_{22}) stresses on the fault elements yield the two di-
 1162 mensional stress tensor. Its Eigenvalues in turn allow for the determinations of
 1163 principle stresses (σ_1 and σ_3). These in turn allow for calculation of the Mohr
 1164 Coulomb stress and the assessment of elements prone to failure in shear according
 1165 to host rocks angle of internal friction (ϕ) and cohesion (c).

$$\tau_m = \sigma_m \sin(\phi) + c \cos(\phi) \quad (11)$$

1166 where,

$$\tau_m = \frac{\sigma_1 - \sigma_3}{2} \quad (12)$$

1167 and,

$$\sigma_m = \frac{\sigma_1 + \sigma_3}{2}. \quad (13)$$

1168 We also assess element that may fail in tension. Elements with least principle
 1169 stress in tension exceeding the cohesive strength of the medium are also identified
 1170 as being prone to fail. In the likely case that entire fault segments (multiple fault
 1171 elements) are in stress conditions exceeding the failure criterion of the rock, we
 1172 choose local maxima of Coulomb stress and tensile stress along these segments as
 1173 the failure points.

1174 This additional functionality is implemented in Matlab and seamlessly links
1175 fric2d, failure assessments and GROW into one single workflow.

1176 **5.1 Model Results**

1177 **6 Discussion**

1178 **6.0.1 Tying the model together with roughness measurements and**
1179 **model**

1180 wear rate (character), tying together model with

1181 **6.1 An external estimate of gouge production and fault**
1182 **thickness * this section will likely be removed**

1183 The data collected in this study offers the unique opportunity to provide new
1184 indirect estimates of fault rock production, fault thickness and dilation rate over
1185 an entire fault. We know that 1) the primordial roughness is systematically rougher
1186 than mature faults, 2) the primordial roughness is relatively constant, and 3) the
1187 roughness can be estimated for a given displacement. Using these results, I will
1188 estimate the volume of fault rock produced through wear and the corresponding
1189 roughness induced accommodation space in the fault system.

1190 Displacing two rough fractal surface in shear requires dilation. The expectation
1191 dilation can be estimated according to the amplitude of the largest wavelength (λ)
1192 being offset (see figure XXX). For a given displacement, u , the largest wavelength
1193 in the system will be $\lambda = 2u_i$. Using a fractal paradigm to define the average
1194 amplitude of a given wavelength according to the pre-factor β and the Hurst

₁₁₉₅ scaling exponent, H , (*reference the equation*) we find that the dilation, A can
₁₁₉₆ be expressed as a function of displacement:

$$A(u) = \sqrt{\beta 2u^{-2H-1}} \quad (14)$$

₁₁₉₇ If we apply this to an entire fault system with displacement field, U , we can
₁₁₉₈ estimate the void space that would be produced:

$$V_{void}(U) = \int_S \sqrt{\beta 2U^{-2H-1}} dS \quad (15)$$

₁₁₉₉ Since the fault system is closed any change in fault roughness *must* be coupled
₁₂₀₀ to the fault core. If all changes in the fault surface are associated with a production
₁₂₀₁ of fault rock, we can effectively estimate the volume of fault rock that has been
₁₂₀₂ produced from displacement u_0 to u_f by comparing the volume integral under the
₁₂₀₃ corresponding initial and final slip surfaces $S(u_0)$ and $S(u_f)$.

$$\frac{\Delta V_{faultrock}}{\Delta u} = \int_S S(u_0) - S(u_f) dS \quad (16)$$

₁₂₀₄ volume integral under the surfaces, S , can be estimated numerically according
₁₂₀₅ to the frequency distribution prescribed by the RMS the entire fault system. Note
₁₂₀₆ that the RMS is estimated at the length scale of the entire fault; wear processes
₁₂₀₇ are active at all length scales below this.

$$\int S dS \approx \quad (17)$$

₁₂₀₈ Now for the displacement field, U , we can estimate the total fault rock produced
₁₂₀₉ by using the primordial surface roughness, $S(0)$, and the prediction of the surface

1210 roughness extrapolated to the length of the fault (* reference the the equation of
1211 smoothing *) such that:

$$V_{fauitrock}(U) = \int_S S(0) - S(U) dS \quad (18)$$

1212 The comparison between the two quatities is telling. If the amount of fault
1213 rock is

1214 7 conclusion

1215 7.1 future work

1216 References

- 1217 [1] Keiiti Aki. Asperities, barriers, characteristic earthquakes and strong motion
1218 prediction. *Journal of Geophysical Research: Solid Earth*, 89(B7):5867–5872,
1219 1984.
- 1220 [2] JeFoa Archard. Contact and rubbing of flat surfaces. *Journal of applied
1221 physics*, 24(8):981–988, 1953.
- 1222 [3] CA Aviles, CH Scholz, and John Boatwright. Fractal analysis applied to
1223 characteristic segments of the san andreas fault. *Journal of Geophysical
1224 Research: Solid Earth*, 92(B1):331–344, 1987.
- 1225 [4] Atilla Aydin. *Faulting in sandstone*. PhD thesis, Stanford, 1977.

- 1226 [5] Atilla Aydin and Arvid M Johnson. Development of faults as zones of defor-
1227 mation bands and as slip surfaces in sandstone. *Pure and applied Geophysics*,
1228 116(4):931–942, 1978.
- 1229 [6] Nir Badt, Yossef H Hatzor, Renaud Toussaint, and Amir Sagy. Geometrical
1230 evolution of interlocked rough slip surfaces: The role of normal stress. *Earth*
1231 and *Planetary Science Letters*, 443:153–161, 2016.
- 1232 [7] Philip Berger and Arvid M Johnson. First-order analysis of deformation of
1233 a thrust sheet moving over a ramp. *Tectonophysics*, 70(3-4):T9–T24, 1980.
- 1234 [8] RL Biegel, W Wang, CH Scholz, and GN BorrNoTr. 1. effects of surface
1235 roughness on initial friction and slip hardening in westerly granite. *Journal*
1236 of *Geophysical Research*, 97(B6):8951–8964, 1992.
- 1237 [9] Andrea Bistacchi, W Ashley Griffith, Steven AF Smith, Giulio Di Toro,
1238 Richard Jones, and Stefan Nielsen. Fault roughness at seismogenic depths
1239 from lidar and photogrammetric analysis. *Pure and Applied Geophysics*,
1240 168(12):2345–2363, 2011.
- 1241 [10] Tom G Blenkinsop. Thickness—displacement relationships for deformation
1242 zones: Discussion. *Journal of Structural Geology*, 11(8):1051–1053, 1989.
- 1243 [11] Elisabeth Bouchaud. Scaling properties of cracks. *Journal of Physics: Con-*
1244 *densed Matter*, 9(21):4319, 1997.
- 1245 [12] Frank Philip Bowden and David Tabor. *The friction and lubrication of solids*,
1246 volume 1. Oxford university press, 2001.

- 1247 [13] Emily E Brodsky, Jacquelyn J Gilchrist, Amir Sagy, and Cristiano Collettini.
1248 Faults smooth gradually as a function of slip. *Earth and Planetary Science*
1249 *Letters*, 302(1):185–193, 2011.
- 1250 [14] Emily E Brodsky, James D Kirkpatrick, and Thibault Candela. Constraints
1251 from fault roughness on the scale-dependent strength of rocks. *Geology*,
1252 44(1):19–22, 2016.
- 1253 [15] Stephen R Brown and Christopher H Scholz. Broad bandwidth study of the
1254 topography of natural rock surfaces. *J. geophys. Res.*, 90(B14):12575–12582,
1255 1985.
- 1256 [16] Roland Bürgmann, David D Pollard, and Stephen J Martel. Slip distribu-
1257 tions on faults: effects of stress gradients, inelastic deformation, heteroge-
1258 neous host-rock stiffness, and fault interaction. *Journal of Structural Geol-*
1259 *ogy*, 16(12):1675–1690, 1994.
- 1260 [17] J Byerlee. Friction, overpressure and fault normal compression. *Geophysical*
1261 *Research Letters*, 17(12):2109–2112, 1990.
- 1262 [18] Jonathan Saul Caine, James P Evans, and Craig B Forster. Fault zone
1263 architecture and permeability structure. *Geology*, 24(11):1025–1028, 1996.
- 1264 [19] Thibault Candela and Emily E Brodsky. The minimum scale of grooving on
1265 faults. *Geology*, 44(8):603–606, 2016.
- 1266 [20] Thibault Candela, François Renard, Michel Bouchon, Alexandre Brouste,
1267 David Marsan, Jean Schmittbuhl, and Christophe Voisin. Characterization
1268 of fault roughness at various scales: Implications of three-dimensional high

- 1269 resolution topography measurements. *Mechanics, Structure and Evolution*
1270 *of Fault Zones*, pages 1817–1851, 2010.
- 1271 [21] Thibault Candela, François Renard, Michel Bouchon, Jean Schmittbuhl, and
1272 Emily E Brodsky. Stress drop during earthquakes: effect of fault roughness
1273 scaling. *Bulletin of the Seismological Society of America*, 101(5):2369–2387,
1274 2011.
- 1275 [22] Thibault Candela, François Renard, Yann Klinger, Karen Mair, Jean Schmit-
1276 tbuhl, and Emily E Brodsky. Roughness of fault surfaces over nine decades
1277 of length scales. *Journal of Geophysical Research: Solid Earth*, 117(B8),
1278 2012.
- 1279 [23] Thibault Candela, François Renard, Jean Schmittbuhl, Michel Bouchon, and
1280 Emily E Brodsky. Fault slip distribution and fault roughness. *Geophysical*
1281 *Journal International*, 187(2):959–968, 2011.
- 1282 [24] G Chambon, J Schmittbuhl, A Corfdir, N Orellana, M Diraison, and
1283 Y Géraud. The thickness of faults: From laboratory experiments to field
1284 scale observations. *Tectonophysics*, 426(1):77–94, 2006.
- 1285 [25] FM Chester and JM Logan. Implications for mechanical properties of brittle
1286 faults from observations of the punchbowl fault zone, California. *Pure and*
1287 *Applied Geophysics*, 124(1-2):79–106, 1986.
- 1288 [26] FM Chester and JM Logan. Composite planar fabric of gouge from the
1289 punchbowl fault, California. *Journal of Structural Geology*, 9(5-6):621IN5–
1290 634IN6, 1987.

- 1291 [27] Frederick M Chester and Judith S Chester. Stress and deformation along
1292 wavy frictional faults. *Journal of Geophysical Research: Solid Earth*,
1293 105(B10):23421–23430, 2000.
- 1294 [28] Frederick M Chester, James P Evans, and Ronald L Biegel. Internal structure
1295 and weakening mechanisms of the san andreas fault. *Journal of Geophysical*
1296 *Research: Solid Earth*, 98(B1):771–786, 1993.
- 1297 [29] Judith S Chester and Raymond C Fletcher. Stress distribution and failure
1298 in anisotropic rock near a bend on a weak fault. *Journal of Geophysical*
1299 *Research: Solid Earth*, 102(B1):693–708, 1997.
- 1300 [30] Michele L Cooke. Fracture localization along faults with spatially varying
1301 friction. *Journal of Geophysical Research: Solid Earth*, 102(B10):22425–
1302 22434, 1997.
- 1303 [31] ML Cooke and DD Pollard. Bedding-plane slip in initial stages of fault-
1304 related folding. *Journal of Structural Geology*, 19(3-4):567–581, 1997.
- 1305 [32] Patience A Cowie and Zoe K Shipton. Fault tip displacement gradients and
1306 process zone dimensions. *Journal of Structural Geology*, 20(8):983–997, 1998.
- 1307 [33] Steven L Crouch and AM Starfield. *Boundary element methods in solid*
1308 *mechanics: with applications in rock mechanics and geological engineering*.
1309 Allen & Unwin, 1982.
- 1310 [34] NC Davatzes and A Aydin. Distribution and nature of fault architecture in
1311 a layered sandstone and shale sequence: An example from the moab fault,
1312 utah. 2005.

- 1313 [35] Nicholas C Davatzes, Atilla Aydin, and Peter Eichhubl. Overprinting fault-
1314 ing mechanisms during the development of multiple fault sets in sandstone,
1315 chimney rock fault array, utah, usa. *Tectonophysics*, 363(1):1–18, 2003.
- 1316 [36] Guy Davidesko, Amir Sagy, and Yossef H Hatzor. Evolution of slip surface
1317 roughness through shear. *Geophysical Research Letters*, 41(5):1492–1498,
1318 2014.
- 1319 [37] James H Dieterich and Deborah Elaine Smith. Nonplanar faults: Mechanics
1320 of slip and off-fault damage. In *Mechanics, Structure and Evolution of Fault*
1321 *Zones*, pages 1799–1815. Springer, 2009.
- 1322 [38] Eric M Dunham, David Belanger, Lin Cong, and Jeremy E Kozdon. Earth-
1323 quake ruptures with strongly rate-weakening friction and off-fault plasticity,
1324 part 2: Nonplanar faults. *Bulletin of the Seismological Society of America*,
1325 101(5):2308–2322, 2011.
- 1326 [39] James T Engelder. Cataclasis and the generation of fault gouge. *Geological*
1327 *Society of America Bulletin*, 85(10):1515–1522, 1974.
- 1328 [40] James P Evans. Thickness-displacement relationships for fault zones. *Jour-*
1329 *nal of structural geology*, 12(8):1061–1065, 1990.
- 1330 [41] Zijun Fang and Eric M Dunham. Additional shear resistance from fault
1331 roughness and stress levels on geometrically complex faults. *Journal of Geo-*
1332 *physical Research: Solid Earth*, 118(7):3642–3654, 2013.
- 1333 [42] Haakon Fossen and Jonny Hesthammer. Deformation bands and their sig-
1334 nificance in porous sandstone reservoirs. *First Break*, 16(1):21–25, 1998.

- 1335 [43] Haakon Fossen, Tord Erlend Skeie Johansen, Jonny Hesthammer, and
1336 Atle Rotevatn. Fault interaction in porous sandstone and implications
1337 for reservoir management; examples from southern utah. *AAPG bulletin*,
1338 89(12):1593–1606, 2005.
- 1339 [44] Haakon Fossen, Richard A Schultz, Zoe K Shipton, and Karen Mair. De-
1340 formation bands in sandstone: a review. *Journal of the Geological Society*,
1341 164(4):755–769, 2007.
- 1342 [45] JA Greenwood and JBP Williamson. Contact of nominally flat surfaces. In
1343 *Proceedings of the Royal Society of London A: Mathematical, Physical and*
1344 *Engineering Sciences*, volume 295, pages 300–319. The Royal Society, 1966.
- 1345 [46] W Ashley Griffith, Stefan Nielsen, Giulio Di Toro, and Steven AF Smith.
1346 Rough faults, distributed weakening, and off-fault deformation. *Journal of*
1347 *Geophysical Research: Solid Earth*, 115(B8), 2010.
- 1348 [47] Christopher Harbord, Stefan Nielsen, and Nicola De Paola. Fault zone rough-
1349 ness controls slip stability. In *EGU General Assembly Conference Abstracts*,
1350 volume 18, page 9799, 2016.
- 1351 [48] Rebecca M Harrington and Emily Brodsky. Smooth, mature faults radiate
1352 more energy than rough, immature faults in parkfield, ca. *Bulletin of the*
1353 *Seismological Society of America*, 99(4):2323–2334, 2009.
- 1354 [49] RR Jones, S Kokkalas, and KJW McCaffrey. Quantitative analysis and
1355 visualization of nonplanar fault surfaces using terrestrial laser scanning (li-
1356 dar)—the arkitsa fault, central greece, as a case study. *Geosphere*, 5(6):465–
1357 482, 2009.

- 1358 [50] Vincent Cooper Kelley and N James Clinton. *Fracture systems and tectonic*
1359 *elements of the Colorado Plateau*. Number 6-7. University of New Mexico
1360 Press, 1960.
- 1361 [51] Bill Kilsdonk and Raymond C Fletcher. An analytical model of hanging-wall
1362 and footwall deformation at ramps on normal and thrust faults. *Tectono-*
1363 *physics*, 163(1-2):153–168, 1989.
- 1364 [52] S Kokkalas, RR Jones, KJW McCaffrey, and P Clegg. Quantitative fault
1365 analysis at arkitsa, central greece, using terrestrial laser-scanning (lidar).
1366 *Bulletin of the Geological Society of Greece*, 37:1–14, 2007.
- 1367 [53] Robert W Krantz. Orthorhombic fault patterns: the odd axis model and
1368 slip vector orientations. *Tectonics*, 8(3):483–495, 1989.
- 1369 [54] RW Krantz. Orthorhombic fault patterns and three-dimensional strain anal-
1370 ysis, northern san rafael swell, utah. In *Geological Society of America Ab-*
1371 *stracts with Programs*, volume 18, page 125, 1986.
- 1372 [55] Thorne Lay, Hiroo Kanamori, and Larry Ruff. *The asperity model and the*
1373 *nature of large subduction zone earthquakes*. na, 1982.
- 1374 [56] Joong-Jeek Lee and Ronald L Bruhn. Structural anisotropy of normal fault
1375 surfaces. *Journal of Structural Geology*, 18(8):1043–1059, 1996.
- 1376 [57] Alan V Levy and Nancy Jee. Unlubricated sliding wear of ceramic materials.
1377 *Wear*, 121(3):363–380, 1988.

- 1378 [58] Laurent Maerten, David D Pollard, and Frantz Maerten. Digital mapping of
1379 three-dimensional structures of the chimney rock fault system, central utah.
1380 *Journal of Structural Geology*, 23(4):585–592, 2001.
- 1381 [59] Benoit B Mandelbrot. Self-affine fractals and fractal dimension. *Physica*
1382 *scripta*, 32(4):257, 1985.
- 1383 [60] Benoit B Mandelbrot, Dann E Passoja, and Alvin J Paullay. Fractal char-
1384 acter of fracture surfaces of metals. 1984.
- 1385 [61] Jessica A McBeck, Elizabeth H Madden, and Michele L Cooke. Growth by
1386 optimization of work (grow): A new modeling tool that predicts fault growth
1387 through work minimization. *Computers & Geosciences*, 88:142–151, 2016.
- 1388 [62] KR McClay and PG Ellis. Analogue models of extensional fault geometries.
1389 *Geological Society, London, Special Publications*, 28(1):109–125, 1987.
- 1390 [63] Brendan J Meade. Algorithms for the calculation of exact displacements,
1391 strains, and stresses for triangular dislocation elements in a uniform elastic
1392 half space. *Computers & geosciences*, 33(8):1064–1075, 2007.
- 1393 [64] HC Meng and KC Ludema. Wear models and predictive equations: their
1394 form and content. *Wear*, 181:443–457, 1995.
- 1395 [65] MS Moreno, J Bolte, J Klotz, and Dr Melnick. Impact of megathrust ge-
1396 ometry on inversion of coseismic slip from geodetic data: Application to the
1397 1960 chile earthquake. *Geophysical Research Letters*, 36(16), 2009.
- 1398 [66] Rodrick Dane Myers. *Structure and hydraulics of brittle faults in sandstone*.
1399 PhD thesis, Stanford University, 1999.

- 1400 [67] Yoshimitsu Okada. Internal deformation due to shear and tensile faults in
1401 a half-space. *Bulletin of the Seismological Society of America*, 82(2):1018–
1402 1040, 1992.
- 1403 [68] Paul G Okubo and James H Dieterich. Effects of physical fault properties on
1404 frictional instabilities produced on simulated faults. *Journal of Geophysical
1405 Research: Solid Earth*, 89(B7):5817–5827, 1984.
- 1406 [69] Kenshiro Otsuki, Nobuaki Monzawa, and Toshiro Nagase. Fluidization and
1407 melting of fault gouge during seismic slip: Identification in the nojima fault
1408 zone and implications for focal earthquake mechanisms. *Journal of Geophys-
1409 ical Research: Solid Earth*, 108(B4), 2003.
- 1410 [70] Andrew Clell Palmer and JR Rice. The growth of slip surfaces in the pro-
1411 gressive failure of over-consolidated clay. In *Proceedings of the Royal Society
1412 of London A: Mathematical, Physical and Engineering Sciences*, volume 332,
1413 pages 527–548. The Royal Society, 1973.
- 1414 [71] William L Power and Terry E Tullis. Euclidean and fractal models for the
1415 description of rock surface roughness. *Journal of Geophysical Research: Solid
1416 Earth*, 96(B1):415–424, 1991.
- 1417 [72] William L Power, Terry E Tullis, and John D Weeks. Roughness and
1418 wear during brittle faulting. *Journal of Geophysical Research: Solid Earth*,
1419 93(B12):15268–15278, 1988.
- 1420 [73] WL Power, TE Tullis, SR Brown, GN Boitnott, and CH Scholz. Roughness
1421 of natural fault surfaces. *Geophysical Research Letters*, 14(1):29–32, 1987.

- 1422 [74] CA Queener, TC Smith, and WL Mitchell. Transient wear of machine parts.
1423 *Wear*, 8(5):391–400, 1965.
- 1424 [75] François Renard, Christophe Voisin, David Marsan, and Jean Schmittbuhl.
1425 High resolution 3d laser scanner measurements of a strike-slip fault quan-
1426 tify its morphological anisotropy at all scales. *Geophysical Research Letters*,
1427 33(4), 2006.
- 1428 [76] Elizabeth Ritz, David D Pollard, and Michael Ferris. The influence of fault
1429 geometry on small strike-slip fault mechanics. *Journal of Structural Geology*,
1430 73:49–63, 2015.
- 1431 [77] Eugene C Robertson et al. Continuous formation of gouge and breccia dur-
1432 ing fault displacement. In *The 23rd US Symposium on Rock Mechanics*
1433 (*USRMS*). American Rock Mechanics Association, 1982.
- 1434 [78] Amir Sagy and Emily E Brodsky. Geometric and rheological asperities in an
1435 exposed fault zone. *Journal of Geophysical Research: Solid Earth*, 114(B2),
1436 2009.
- 1437 [79] Amir Sagy, Emily E Brodsky, and Gary J Axen. Evolution of fault-surface
1438 roughness with slip. *Geology*, 35(3):283–286, 2007.
- 1439 [80] Francois Saucier, Eugene Humphreys, and Ray Weldon. Stress near geo-
1440 metrically complex strike-slip faults: application to the san andreas fault
1441 at cajon pass, southern california. *Journal of Geophysical Research: Solid*
1442 *Earth*, 97(B4):5081–5094, 1992.

- 1443 [81] Heather M Savage and Michele L Cooke. Unlocking the effects of friction on
1444 fault damage zones. *Journal of Structural Geology*, 32(11):1732–1741, 2010.
- 1445 [82] Jean Schmittbuhl, Sylvie Gentier, and Stéphane Roux. Field measurements
1446 of the roughness of fault surfaces. *Geophysical Research Letters*, 20(8):639–
1447 641, 1993.
- 1448 [83] Jean Schmittbuhl, Francois Schmitt, and Christopher Scholz. Scaling in-
1449 variance of crack surfaces. *Journal of Geophysical Research: Solid Earth*,
1450 100(B4):5953–5973, 1995.
- 1451 [84] Jean Schmittbuhl, Jean-Pierre Vilotte, and Stéphane Roux. Reliability of
1452 self-affine measurements. *Physical Review E*, 51(1):131, 1995.
- 1453 [85] CH Scholz and JT Engelder. The role of asperity indentation and ploughing
1454 in rock friction—i: Asperity creep and stick-slip. In *International Journal of*
1455 *Rock Mechanics and Mining Sciences & Geomechanics Abstracts*, volume 13,
1456 pages 149–154. Elsevier, 1976.
- 1457 [86] Ch H Scholz and CA Aviles. The fractal geometry of faults and faulting.
1458 *Earthquake source mechanics*, pages 147–155, 1986.
- 1459 [87] Christopher H Scholz. Wear and gouge formation in brittle faulting. *Geology*,
1460 15(6):493–495, 1987.
- 1461 [88] Richard A Schultz and Haakon Fossen. Displacement-length scaling in three
1462 dimensions: the importance of aspect ratio and application to deformation
1463 bands. *Journal of Structural Geology*, 24(9):1389–1411, 2002.

- 1464 [89] Paul Segall and DD Pollard. Mechanics of discontinuous faults. *Journal of*
1465 *Geophysical Research: Solid Earth*, 85(B8):4337–4350, 1980.
- 1466 [90] Katherine AH Shervais and James D Kirkpatrick. Smoothing and re-
1467 roughening processes: The geometric evolution of a single fault zone. *Journal*
1468 *of Structural Geology*, 91:130–143, 2016.
- 1469 [91] Zheqiang Shi and Steven M Day. Rupture dynamics and ground motion from
1470 3-d rough-fault simulations. *Journal of Geophysical Research: Solid Earth*,
1471 118(3):1122–1141, 2013.
- 1472 [92] ZK Shipton and PA Cowie. Damage zone and slip-surface evolution over μm
1473 to km scales in high-porosity navajo sandstone, utah. *Journal of Structural*
1474 *Geology*, 23(12):1825–1844, 2001.
- 1475 [93] Zoe K Shipton and Patience A Cowie. A conceptual model for the origin of
1476 fault damage zone structures in high-porosity sandstone. *Journal of Struc-*
1477 *tural Geology*, 25(3):333–344, 2003.
- 1478 [94] Zoe K Shipton, James P Evans, Kim R Robeson, Craig B Forster, and
1479 Stephen Snelgrove. Structural heterogeneity and permeability in faulted
1480 eolian sandstone: Implications for subsurface modeling of faults. *AAPG*
1481 *bulletin*, 86(5):863–883, 2002.
- 1482 [95] Zoe K Shipton, Aisling M Soden, James D Kirkpatrick, Aileen M Bright,
1483 and Rebecca J Lunn. How thick is a fault? fault displacement-thickness
1484 scaling revisited. *Earthquakes: Radiated energy and the physics of faulting*,
1485 pages 193–198, 2006.

- 1486 [96] RH Sibson. Fault rocks and fault mechanisms. *Journal of the Geological*
1487 *Society*, 133(3):191–213, 1977.
- 1488 [97] Richard H Sibson. Crustal stress, faulting and fluid flow. *Geological Society,*
1489 *London, Special Publications*, 78(1):69–84, 1994.
- 1490 [98] Mark W Stirling, Steven G Wesnousky, and Kunihiko Shimazaki. Fault
1491 trace complexity, cumulative slip, and the shape of the magnitude-frequency
1492 distribution for strike-slip faults: a global survey. *Geophysical Journal In-*
1493 *ternational*, 124(3):833–868, 1996.
- 1494 [99] R Summers and J Byerlee. A note on the effect of fault gouge composition on
1495 the stability of frictional sliding. In *International Journal of Rock Mechanics*
1496 and *Mining Sciences & Geomechanics Abstracts*, volume 14, pages 155–160.
1497 Elsevier, 1977.
- 1498 [100] Mark T Swanson. Sidewall ripouts in strike-slip faults. *Journal of Structural*
1499 *Geology*, 11(8):933–948, 1989.
- 1500 [101] Anita Torabi and Haakon Fossen. Spatial variation of microstructure and
1501 petrophysical properties along deformation bands in reservoir sandstones.
1502 *AAPG bulletin*, 93(7):919–938, 2009.
- 1503 [102] Peter Vrolijk, Rod Myers, Michael L Sweet, Zoe K Shipton, Ben Dock-
1504 rill, James P Evans, Jason Heath, and Anthony P Williams. Anatomy of
1505 reservoir-scale normal faults in central utah: Stratigraphic controls and im-
1506 plications for fault zone evolution and fluid flow. *Field Guides*, 6:261–282,
1507 2005.

- 1508 [103] Weibin Wang and Christopher H Scholz. Wear processes during frictional
1509 sliding of rock: a theoretical and experimental study. *JOURNAL OF GEO-*
1510 *PHYSICAL RESEARCH-ALL SERIES-*, 99:6789–6789, 1994.
- 1511 [104] Naoto YOSHIOKA. Fracture energy and the variation of gouge and surface
1512 roughness during frictional sliding of rocks. *Journal of Physics of the Earth*,
1513 34(4):335–355, 1986.
- 1514 [105] O Zielke, M Galis, and PM Mai. Fault roughness and strength heterogene-
1515 ity control earthquake size and stress drop. *Geophysical Research Letters*,
1516 44(2):777–783, 2017.
- 1517 [106] Olaf Zielke and Paul Martin Mai. Sub-patch roughness in earthquake rupture
1518 investigations. *Geophysical Research Letters*, 2016.

1519 **8 Appendix**

1520 **8.1 Surface Processing scripts**

1521 Or possibly a link to a git repository...

1522 **8.2 User manual for script**

1523 This manual should serve as both a basic guide to the logic and usage of the *surface*
1524 *processing package*.

1525 The master function of the package is *surfaceprocessing*. This function effec-
1526 tively deal with the inputs and direct computations towards the necessary func-
1527 tions. Outputs of the function are a .mat workspace file for each input data file.

1528 The workspace includes a structure (called *parameters*) with the raw surface anal-
1529 ysis outputs, the point spacing, the decimation factor (if any), the file name and
1530 the date of the analysis. The workspace also includes the grid form of the origi-
1531 nal inputed surface (called *surface*), and the pre-processed copy that was used for
1532 the subsequent analysis (called *zGrid*). Inputs are always included in pairs. The
1533 former defines the type of input, the latter qualifies or quantifies the input. This
1534 structure allows for adaptability of the code to various needs. Options include the
1535 following:

1536 • *what to do?*: 'toDo', followed by the desired analyses on of: 'FFT', 'PLOMB',
1537 'parameters' or 'all' (default is 'all') - can be a cell array. This specifies what
1538 kind of spatial analysis will be done on the input surface data. The spatial
1539 analysis is calculated and averaged across every single profiles along the
1540 surface. The analyses are the following:

- 1541 – 'FFT', a power spectrum computed using a Fast Fourier Transform
1542 (FFT) algorithm;
- 1543 – 'PLOMB', a power spectrum computed using a least-squares Lomb-
1544 Scargle algorithm;
- 1545 – 'paramters', the calculation (as a function of scale) of the Root Mean
1546 Squared (RMS), skewness, kurtosis and asymmetry averaged across all
1547 segments of a given length on all profiles of the surface.

1548 'all' simply performs all the analyses outlined above.

- 1549 • *skip pre-processing?*: 'bypass', followed by 'zygo', 'pre-processing' or 'no' to
1550 be used input is already in aligned clean grid form - input files are then

1551 (default is 'no'). 'zygo' is specifically adapted to the proprietary data format
1552 of the white light in Wong. 'pre-processing' simply skips any pre-processing.
1553 This option requires a .mat structure with a field named 'grid' with the
1554 topography and a field name 'pointSpacing' specifying the point spacing (in
1555 meters). In either case the topography must be aligned such that the positive
1556 x direction is the parallel direction.

1557 • *for the parameter analysis, how many scales?* 'numberOfScales' followed
1558 by the desired number of analysed scales. This option is relevant to the
1559 parameters analysis. Note that this has a lot of effect on the amount of
1560 processing time (default is 10).

1561 • *decimation:* 'decimationFactor' followed by the desired decimation factor
1562 (default is 1). Decimation is a useful tool to reduce computation time. The
1563 surface grid is sub-sampled according to the decimation such that a decima-
1564 tion factor of k would imply that only every k th point on the every k th will
1565 be considered for hte subsequent analysis.

1566 • *Instrument specific analysis* 'instrument' followed by 'white light', 'laser
1567 scanner' or 'lidar' (default does not set any instrument specific adjustments).
1568 Some instrument specific pre-processing steps are taken. Please contact me
1569 if you intend to use this as they may be highly dependent on the specific
1570 instrument used.

1571 For instance, *surfaceprocessing('todo','FFT','bypass','zygo')* will only perform
1572 a power spectral density analysis and will skip preprocessing and assume that all
1573 input will be in the 'zygo' export .xyz format.

1574 When the command is executed, the user will be prompted to navigate to the
1575 directory where the input data is located. IMPORTANT: the directory must *only*
1576 contain files of one data format. There cannot be other files or sub-directories
1577 in the directory. The user will then be prompted to choose a destination for the
1578 output data. The requirements for the output location are less stringent. However,
1579 it is advisable to choose an empty directory such as to facilitate subsequent steps.

1580 The next step is to visualize the output of the analysis. This is done using the
1581 *unpack parameters* function. This function provides various visualization options
1582 for all files in the directory chosen by the user. The first input (the *desired plot*)
1583 can be one of the following:

1584 'FFT': plot all power spectra;

1585 'PLOMB': periodogram plot as determined by the Lomb-Scargle least squares
1586 analysis;

1587 'topostd': plot of the root mean squared (RMS) as a function of scale;

1588 'topoSkew': plot of skewness of height fields as a function of segment scale;

1589 'topoKurt': plot of the the kurtoisis of height fields as a function of segment
1590 scale;

1591 'PowerVsDisp': plot of power interpolated at a given scale as a function of
1592 displacement;

1593 'RMSVsDisp': model RMS at a given scale as a function of displacement

1594 'Grids': shows both the original and pre-processed grid for the specified file
1595 'fileName';

1596 '*Best Fits*': best logarithmic fits to power spectra obtained from the fast
1597 fourrier transform analysis.

1598 The functionality of the packages is broadly divided into three sections: 1)
1599 importing and preprocessing data, 2) performing various spatial statistics on the
1600 pre-processed data, and 3) unpacking the analysis output into figures.

1601 In order to run smoothly the all functions included in the package should be
1602 kept in the same directory or on an accessible path.

1603 For reference, here is a quick outline of what each function does:

1604 *affine fit*: (from mathworks) Computes the plane of best fit using least
1605 squares normal distance;

1606 *align grid*: finds the smoothest directions in a grid using FFT spectra and
1607 rotates and re-grids the input grid;

1608 *fault spectral density simple*: Calculates the average lomb-scargle spectral
1609 density every row of a N by M array;

1610 *FindErr loop anisotropy*

1611 *flatten XYZ*: removes planar trends from XYZ data by applying a rotations
1612 matrix according to the best fit plane (*affine fit*);

1613 *fractal model outlier*: Removes outlying segments according to a near-gaussian
1614 model for the distribution of RMS values at specified segment lengths (or
1615 scales);

1616 *frequency spectrum*: Calculates the average lomb-scargle spectral density of
1617 all continuous segments on every single row of a N by M array;

1618 *parse 'zygo' format*: extracts the both the point spacing and topographic grid
1619 from the exported zygo format. Can also remove planar trend from data
1620 (substracted from grid);

1621 *rotateZ*: applies rotation matrix on XYZ data

1622 *surface 'analysis'*: Aggregates the analysis functions and applies them to an
1623 input grid

1624 *surface 'cleaning'*: removes outliers associated with surface defects

1625 *surface 'parameters'*: calculates spatial statistics and parameters along seg-
1626 ments as a function of scale (RMS, skewness, directional asymmetry and
1627 kurtosis)

1628 *surface 'preprocessing' 2*: deals with preprocessing input data (import data,
1629 cleaning and gridding data)

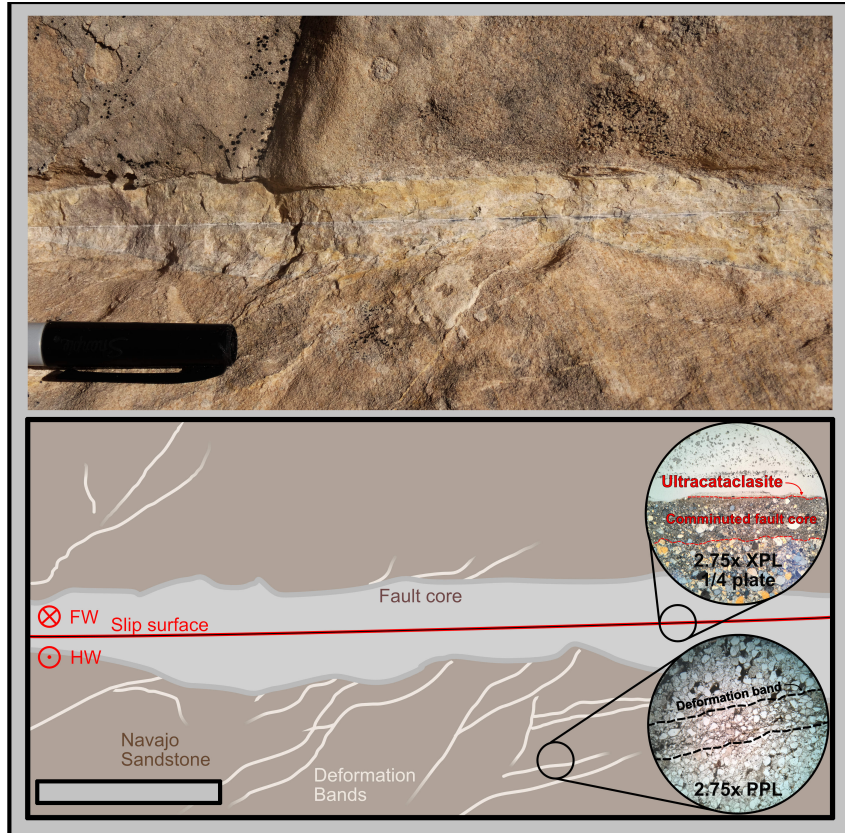


Figure 4: Top: Example of representative meso-structure of faults in the Navajo sandstone. Bottom: Cartoon of the representative meso-structure with slip surface (red), fault core (grey), deformation bands (pale beige) and intact host sand stone (brown). Upper half is the footwall; lower half is the hanging wall. Exposure is slip perpendicular. Representative thin sections show (not in situ) show the bottom half of the fault core (top) and deformation band (bottom). The section through the slip surface shows the microstructural architecture of slip surfaces with a very fine layer (barely visible) of ultracataclasite and a bounding comminuted layer. Note that this section is still well within the fault core. The section through the deformation bands shows the gradational reduction in grain size (outlined by black dashed line).

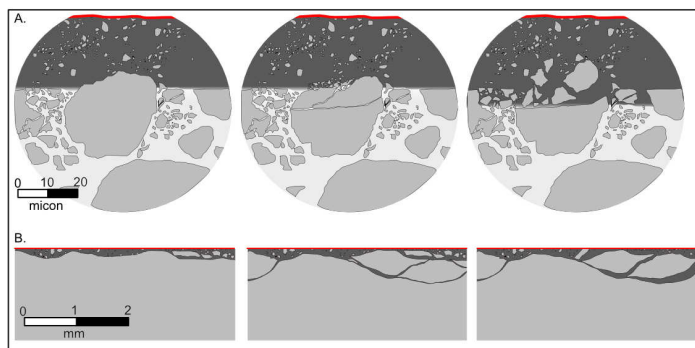


Figure 5: Schematic example of the interface between the cataclastic host and the fluidized ultracataclasite layer at two distinct length scales. A. at the length scale of ten's of microns grains, the shape of the interface is



Figure 6: Example of a slip surface interpreted as a principle slip surface with around 20 meters of displacement at Big Hole Fault



Figure 7: Left: Example of at least two distinct polished slip surfaces on the same fault structure. Right: Example of concentric pattern on cross-sectional view a fault

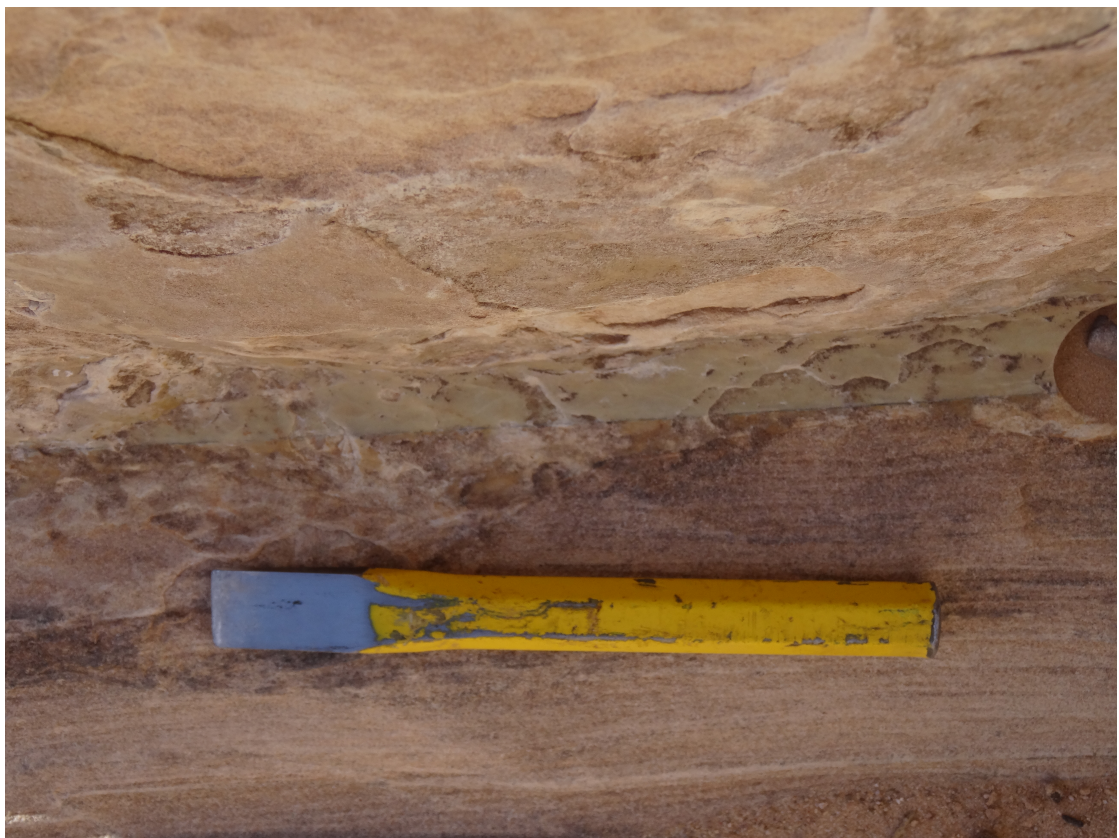


Figure 8: Example of a slip surface interpreted as a principle slip surface with around 20 meters of displacement at Big Hole Fault

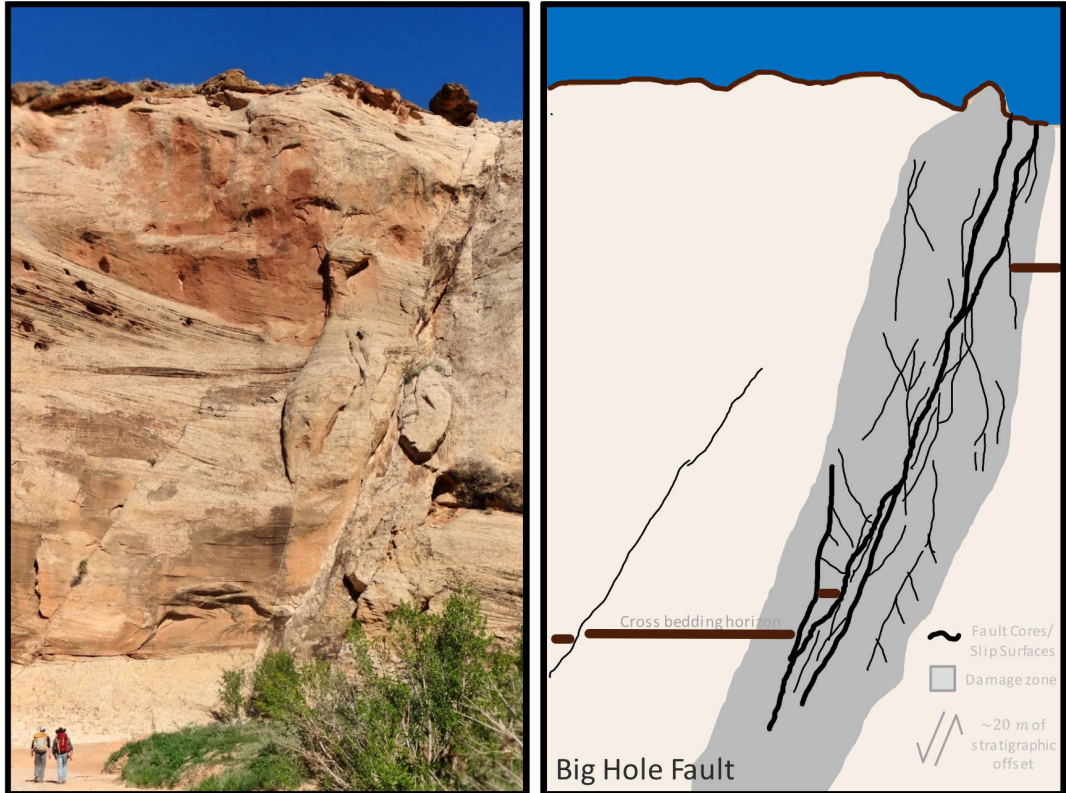


Figure 9: At Big Hole fault, two large-scale continuous strands of the fault, both accommodating meters of displacement exemplify problem at a larger scale. Due to the ambiguity, Shipton and Cowie, 2003 report large uncertainty on the partitioning of stratigraphic offset across the two strand

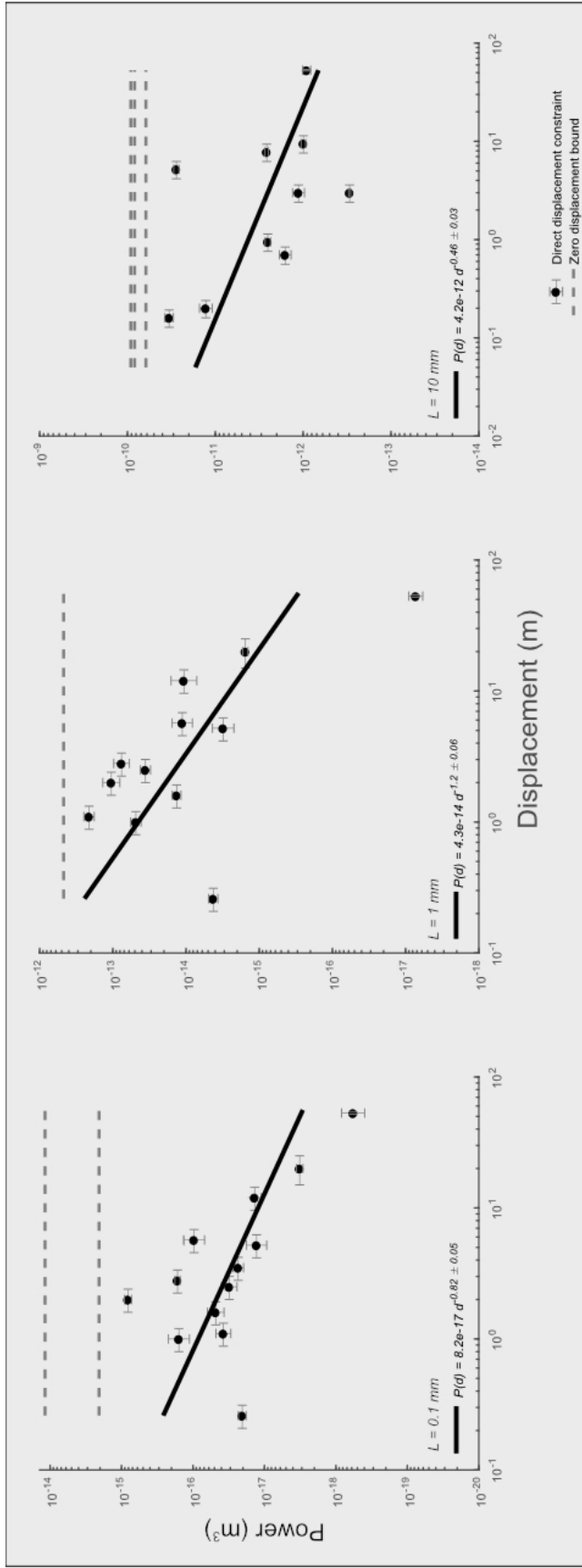


Figure 10: Roughness as a function of displacement at various scales (100 μm , 1 mm , and 1 cm). Best fit line indicated in black. Roughness of joints and/or deformation bands indicated with grey dashed line.

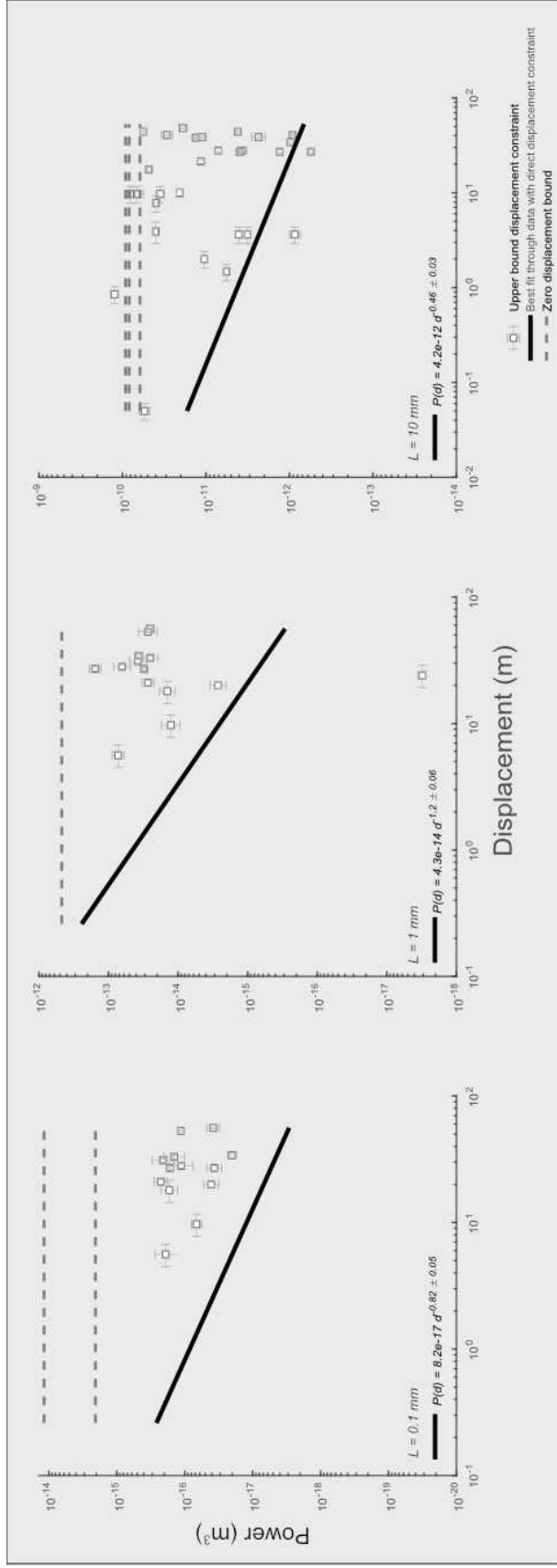


Figure 11: Roughness of faults with only maximum constraints on displacement as a function of displacement at various scales ($100 \mu\text{m}$, 1 mm , and 1 cm) compared to best fit through data with direct constraints on displacement. Best fit line indicated in black. Roughness of joints and/or deformation bands indicated with grey dashed line. Note that with the exception of a few outliers, the points with x -axes defined by maximum allowable displacement all obey the inequality physically required by the smoothing model best fit.